



ATLAS Note

GROUP-2017-XX

10th November 2020



A Deep Learning Approach to Differential Measurements of $t\bar{t}H$ Production in Multilepton Final States

The ATLAS Collaboration

The possibility of using the kinematic properties of the Higgs boson to search for new physics is investigated using $t\bar{t}H$ events with multiple leptons in the final state. Because of the challenges inherent to reconstructing the Higgs in multilepton final states, a deep learning approach is used to reconstruct the momentum spectrum of the Higgs, which would be altered by the presence of new physics without affecting the overall rate of $t\bar{t}H$ production. Simulations representing 139 fb^{-1} at $\sqrt{s} = 13 \text{ TeV}$ are used to provide estimates of the sensitivity to variations in the Higgs p_T spectrum.

¹³ © 2020 CERN for the benefit of the ATLAS Collaboration.

¹⁴ Reproduction of this article or parts of it is allowed as specified in the CC-BY-4.0 license.

15 **Contents**

16	1 Changes and outstanding items	4
17	1.1 Changelog	4
18	2 Introduction	5
19	3 Data and Monte Carlo Samples	5
20	3.1 Data Samples	6
21	3.2 Monte Carlo Samples	6
22	4 Object Reconstruction	7
23	4.1 Trigger Requirements	7
24	4.2 Light Leptons	7
25	4.3 Jets	8
26	4.4 Missing Transverse Energy	9
27	5 Higgs Momentum Reconstruction	9
28	5.1 Decay Candidate Reconstruction	9
29	5.2 b-jet Identification	10
30	5.3 Higgs Reconstruction	13
31	5.4 p_T Prediction	21
32	5.5 3l Decay Mode	26
33	6 Signal Region Definitions	28
34	6.1 Pre-MVA Event Selection	28
35	6.2 Event MVA	29
36	6.3 Signal Region Definitions	34
37	7 Systematic Uncertainties	36
38	8 Results	38
39	8.1 Results - 80 fb^{-1}	38
40	8.2 Projected Results - 140 fb^{-1}	39
41	9 Conclusion	39
42	Appendices	44
43	A Machine Learning Models	44
44	A.1 Higgs Reconstruction Models	44
45	A.2 Background Rejection MVAs	67
46	A.3 Alternate b-jet Identification Algorithm	76
47	A.4 Binary Classification of the Higgs p_T	76

⁴⁹ **1 Changes and outstanding items**

⁵⁰ **1.1 Changelog**

⁵¹ This is version 1

52 2 Introduction

53 Since the discovery of a Higgs boson compatible with the Standard Model (SM) in 2012 [], its
 54 interactions with other particles have been studied using proton-proton collision data produced by
 55 the Large Hadron Collider (LHC). The strongest of these interactions is the coupling of the Higgs
 56 to the top quark, making the Yukawa coupling between these two particles of particular interest
 57 for study.

58 These interactions can be measured directly by studying the production of a Higgs Boson in
 59 association with a pair of Top Quarks ($t\bar{t}H$) []. While this process has been observed by both
 60 the ATLAS [] and CMS [] collaborations, these analyses have focused on measuring the overall
 61 rate of $t\bar{t}H$ production. There are several theories of physics Beyond the Standard Model (BSM),
 62 however, that would affect the kinematics of $t\bar{t}H$ production without altering its overall rate [].

63 An Effective Field Theory approach can be used to model the low energy effects of new, high
 64 energy physics, by parameterizing BSM effects as dimension-six operators. The addition of these
 65 operators can be shown to modify the transverse momentum (p_T) spectrum of the Higgs Boson [].
 66 Therefore, reconstructing the momentum spectrum of the Higgs provides a means to observe new
 67 physics in the Higgs sector.

68 This note reports on the feasibility of measuring the impact of dimension-six operators in $t\bar{t}H$
 69 events with multiple leptons in the final state, using Monte Carlo (MC) simulations scaled to
 70 139 fb^{-1} at an energy $\sqrt{s} = 13 \text{ TeV}$. Events are separated into channels based on the number
 71 of light leptons (electrons and muons) in the final state - either two same-sign leptons (2lSS),
 72 or three leptons (3l). A deep neural network is used to identify which objects originate from
 73 the decay of the Higgs, and reconstruct the momentum of the Higgs Boson in each event. This
 74 reconstructed momentum spectrum is used to place limits on BSM effects, and on the parameters
 75 of dimension-six operators.

76 This note is organized as follows: Section ?? describes the LHC and the ATLAS detector. The
 77 dataset and Monte Carlo (MC) simulations used in the analysis is outlined in section 3. Section 4
 78 describes the identification and reconstruction of the various physics objects. The models used to
 79 reconstruct the momentum spectrum of the Higgs is discussed in section 5. The selection and
 80 categorisation of events comprises section 6, and the theoretical and experimental systematic
 81 uncertainties considered are described in section 7. Finally, the results of the study are summarized
 82 in section 8.

83 3 Data and Monte Carlo Samples

84 For both data and Monte Carlo (MC) simulations, samples were prepared in the xAOD format,
 85 which was used to produce a xAOD based on the HIGG8D1 derivation framework. This framework
 86 was designed for the main $t\bar{t}H$ multi-lepton analysis. Because this analysis targets events with

87 multiple light leptons, as well as tau hadrons, this framework skims the dataset of any events that
 88 do not meet at least one of the following requirements:

- 89 • at least two light leptons within a range $|\eta| < 2.6$, with leading lepton $p_T > 15$ GeV and
 90 subleading lepton $p_T > 5$ GeV
 91 • at least one light lepton with $p_T > 15$ GeV within a range $|\eta| < 2.6$, and at least two hadronic
 92 taus with $p_T > 15$ GeV.

93 Samples were then generated from these HIGG8D1 derivations using a modified version of
 94 AnalysisBase version 21.2.127.

95 **3.1 Data Samples**

96 The study uses proton-proton collision data collected by the ATLAS detector from 2015 through
 97 2018, which represents an integrated luminosity of 139 fb^{-1} and an energy of $\sqrt{s} = 13 \text{ TeV}$. All
 98 data used in this analysis was included in one of the following Good Run Lists:

- 99 • data15_13TeV.periodAllYear_DetStatus-v79-repro20-02_DQDefects-00-02-02
 100 _PHYSGRL_All_Good_25ns.xml
 101 • data16_13TeV.periodAllYear_DetStatus-v88-pro20-21_DQDefects-00-02-04
 102 _PHYSGRL_All_Good_25ns.xml
 103 • data17_13TeV.periodAllYear_DetStatus-v97-pro21-13_Unknown_PHYSGRL
 104 _All_Good_25ns_Triggerno17e33prim.xml
 105 • data18_13TeV.periodAllYear_DetStatus-v102-pro22-04_Unknown_PHYSGRL
 106 _All_Good_25ns_Triggerno17e33prim.xml

107 **3.2 Monte Carlo Samples**

108 Several Monte Carlo (MC) generators were used to simulate both signal and background processes.
 109 For all of these, the effects of the ATLAS detector are simulated in Geant4. The specific event
 110 generator used for each of these MC samples is listed in table 1.

Table 1: The configurations used for event generation of signal and background processes, including the event generator, matrix element (ME) order, parton shower algorithm, and parton distribution function (PDF).

Process	Event generator	ME order	Parton Shower	PDF
t̄H	MG5_AMC (MG5_AMC)	NLO (NLO)	PYTHIA 8 (HERWIG++)	NNPDF 3.0 NLO [Ball:2014uwa] (CT10 [ct10])
t̄W	MG5_AMC (SHERPA 2.1.1)	NLO (LO multileg)	PYTHIA 8 (SHERPA)	NNPDF 3.0 NLO (NNPDF 3.0 NLO)
t̄(Z/γ* → ll)	MG5_AMC	NLO	PYTHIA 8	NNPDF 3.0 NLO
VV	SHERPA 2.2.2	MEPS NLO	SHERPA	CT10
t̄t	POWHEG-BOX v2 [powheggtt]	NLO	PYTHIA 8	NNPDF 3.0 NLO
t̄γ	MG5_AMC	LO	PYTHIA 8	NNPDF 2.3 LO
tZ	MG5_AMC	LO	PYTHIA 6	CTEQ6L1
tHqb	MG5_AMC	LO	PYTHIA 8	CT10
tHW	MG5_AMC (SHERPA 2.1.1)	NLO (LO multileg)	HERWIG++ (SHERPA)	CT10 (NNPDF 3.0 NLO)
tWZ	MG5_AMC	NLO	PYTHIA 8	NNPDF 2.3 LO
t̄t, t̄t̄t̄	MG5_AMC	LO	PYTHIA 8	NNPDF 2.3 LO
t̄tW+W-	MG5_AMC	LO	PYTHIA 8	NNPDF 2.3 LO
s-, t-channel, Wt single top	Powheg-BOX v1 [powhegstp]	NLO	PYTHIA 6	CT10
qqVV, VVV				
Z → l+l-	SHERPA 2.2.1	MEPS NLO	SHERPA	NNPDF 3.0 NLO

4 Object Reconstruction

All analysis channels considered in this note share a common object selection for leptons and jets, as well as a shared trigger selection.

4.1 Trigger Requirements

Events are required to be selected by dilepton triggers, as summarized in table 2.

4.2 Light Leptons

Electron candidates are reconstructed from energy clusters in the electromagnetic calorimeter that are associated with charged particle tracks reconstructed in the inner detector [[ATLAS-CONF-2016-024](#)]. Electron candidates are required to have $p_T > 10$ GeV and $|\eta_{\text{cluster}}| < 2.47$. Candidates in the transition region between different electromagnetic calorimeter components, $1.37 < |\eta_{\text{cluster}}| < 1.52$, are rejected. A multivariate likelihood discriminant combining shower shape and track information is used to distinguish prompt electrons from nonprompt leptons, such as those originating from hadronic showers.

Dilepton triggers (2015)	
$\mu\mu$ (asymm.)	HLT_mu18_mu8noL1
ee (symm.)	HLT_2e12_lhloose_L12EM10VH
$e\mu, \mu e$ (\sim symm.)	HLT_e17_lhloose_mu14
Dilepton triggers (2016)	
$\mu\mu$ (asymm.)	HLT_mu22_mu8noL1
ee (symm.)	HLT_2e17_lhvloose_nod0
$e\mu, \mu e$ (\sim symm.)	HLT_e17_lhloose_nod0_mu14
Dilepton triggers (2017)	
$\mu\mu$ (asymm.)	HLT_mu22_mu8noL1
ee (symm.)	HLT_2e24_lhvloose_nod0
$e\mu, \mu e$ (\sim symm.)	HLT_e17_lhloose_nod0_mu14
Dilepton triggers (2018)	
$\mu\mu$ (asymm.)	HLT_mu22_mu8noL1
ee (symm.)	HLT_2e24_lhvloose_nod0
$e\mu, \mu e$ (\sim symm.)	HLT_e17_lhloose_nod0_mu14

Table 2: List of lowest p_T -threshold, un-prescaled dilepton triggers used for 2015–2018 data taking.

124 To further reduce the non-prompt contribution, the track of each electron is required to originate
125 from the primary vertex; requirements are imposed on the transverse impact parameter significance
126 ($|d_0|/\sigma_{d_0}$) and the longitudinal impact parameter ($|\Delta z_0 \sin \theta_\ell|$), as shown in table ??.

127 Muon candidates are reconstructed by combining inner detector tracks with track segments or
128 full tracks in the muon spectrometer **[PERF-2014-05]**. Muon candidates are required to have
129 $p_T > 10$ GeV and $|\eta| < 2.5$. All leptons are required to be isolated, and pass a non-prompt BDT
130 selection described in detail in **[ttH_paper]**.

131 4.3 Jets

132 Jets are reconstructed from calibrated topological clusters built from energy deposits in the
133 calorimeters **[ATL-PHYS-PUB-2015-015]**, using the anti- k_t algorithm with a radius parameter
134 $R = 0.4$. Jets with energy contributions likely arising from noise or detector effects are removed
135 from consideration **[ATLAS-CONF-2015-029]**, and only jets satisfying $p_T > 25$ GeV and
136 $|\eta| < 2.5$ are used in this analysis. For jets with $p_T < 60$ GeV and $|\eta| < 2.4$, a jet-track association
137 algorithm is used to confirm that the jet originates from the selected primary vertex, in order to
138 reject jets arising from pileup collisions **[PERF-2014-03]**.

¹³⁹ **4.4 Missing Transverse Energy**

¹⁴⁰ Because all $t\bar{t}H$ – ML channels considered include multiple neutrinos, missing transverse energy
¹⁴¹ (E_T^{miss}) is present in each event. The missing transverse momentum vector is defined as the
¹⁴² inverse of the sum of the transverse momenta of all reconstructed physics objects as well as
¹⁴³ remaining unclustered energy, the latter of which is estimated from low- p_T tracks associated with
¹⁴⁴ the primary vertex but not assigned to a hard object [ATL-PHYS-PUB-2015-027].

¹⁴⁵ **5 Higgs Momentum Reconstruction**

¹⁴⁶ Reconstructing the momentum of the Higgs boson is a particular challenge for channels with
¹⁴⁷ leptons in the final state: Because all channels include at least two neutrinos in the final state, the
¹⁴⁸ Higgs can never be fully reconstructed. However, the momentum spectrum can be well predicted
¹⁴⁹ by a neural network when provided with the four-vectors of the Higgs Boson decay products, as
¹⁵⁰ shown in section 5.1. With this in mind, several layers of MVAs are used to reconstruction the
¹⁵¹ Higgs momentum.

¹⁵² The first layer is a model designed to select which jets are most likely to be the b-jets that came
¹⁵³ from the top decay, detailed in section 5.2. As described in section 5.3, the kinematics of these
¹⁵⁴ jets are fed into the second layer, which is designed to identify the decay products of the Higgs
¹⁵⁵ Boson itself. The kinematics of these particles are then fed into yet another neural-network, which
¹⁵⁶ predicts the momentum of the Higgs (5.4). MVAs are also used in the analysis to determine the
¹⁵⁷ decay of the Higgs boson in the 3l channel (5.5).

¹⁵⁸ Models are trained on Monte Carlo simulations of $t\bar{t}H$ events generated using MG5_AMC.
¹⁵⁹ Specifically, events DSIDs 346343-5, 345873-5, and 345672-4 are used for training.

¹⁶⁰ For all of these models, the Keras neural network framework, with Tensorflow as the backend, is
¹⁶¹ used, and the number of hidden layers and nodes are determined using grid search optimization.
¹⁶² Each neural network uses the LeakyReLU activation function, a learning rate of 0.01, and the
¹⁶³ Adam optimization algorithm, as alternatives are found to either decrease or have no impact on
¹⁶⁴ performance. Batch normalization is applied after each layer. For the classification algorithms
¹⁶⁵ (b-jet matching, Higgs reconstruction, and 3l decay identification) binary-cross entropy is used as
¹⁶⁶ the loss function, while the p_T reconstruction algorithm uses MSE.

¹⁶⁷ The specific inputs features used for each model are arrived at through a process of trial and error
¹⁶⁸ - features considered potentially useful are tried, and those that are found to increase performance
¹⁶⁹ are included. While each model includes a relatively large number of features, some using
¹⁷⁰ upwards of 30, this inclusive approach is found to maximize the performance of each model while
¹⁷¹ decreasing the variance compared to a reduced number of inputs. Each input feature is validated
¹⁷² by comparing MC simulations to 80 fb^{-1} of data, as shown in the sections below.

¹⁷³ **5.1 Decay Candidate Reconstruction**

¹⁷⁴ Machine Learning algorithms are trained to identify the decay products of the Higgs Boson using
¹⁷⁵ MC simulations of $t\bar{t}H$ events. These include light leptons and jets. Reconstructed physics
¹⁷⁶ objects are matched to truth level particles, in order to identify the parents of these reconstructed
¹⁷⁷ objects. The kinematics of the decay product candidates as well as event level variables are used
¹⁷⁸ as inputs.

¹⁷⁹ Leptons considered as possible Higgs and top decay candidates are required to pass the selection
¹⁸⁰ described in section 4.2. For jets, however, it is found that a large fraction that originate from either
¹⁸¹ the top decay or the Higgs decay fall outside the selection described in section 4.3. Specifically,
¹⁸² jets from the Higgs decay tend to be soft, with 32% having $p_T < 25$ GeV. Therefore jets with
¹⁸³ $p_T < 15$ GeV are considered as possible candidates in the models described below. By contrast,
¹⁸⁴ less than 5% of the jets originating from the Higgs fall below this p_T . The jets are found to be
¹⁸⁵ well modeled even down to this low p_T threshold, as shown in section 6.1. The impact of using
¹⁸⁶ different p_T selection for the jet candidates is considered in detail in section A.5. As they are
¹⁸⁷ expected to originate from the primary vertex, jets are also required to pass a JVT cut.

¹⁸⁸ **5.2 b-jet Identification**

¹⁸⁹ Including the kinematics of the b-jets that originate from the top decay is found to improve the
¹⁹⁰ identification of the Higgs decay products, and improve the accuracy with which the Higgs
¹⁹¹ momentum can be reconstructed. Because these b-jets are reconstructed by the detector with high
¹⁹² efficiency (just over 90% of the time), and can be identified relatively consistently, the first step in
¹⁹³ reconstructing the Higgs is selecting the b-jets from the top decay.

¹⁹⁴ Exactly two b-jets are expected in the final state of $t\bar{t}H - ML$ events. However, in both the 3l and
¹⁹⁵ 2lSS channels, only one or more b-tagged jets are required (where the 70% DL1r b-tag working
¹⁹⁶ point is used). Therefore, for events which have exactly one, or more than two, b-tagged jets,
¹⁹⁷ deciding which combination of jets correspond to the top decay is non-trivial. Further, events
¹⁹⁸ with 1 b-tagged jet represent just over half of all $t\bar{t}H - ML$ events. Of those, both b-jets are
¹⁹⁹ reconstructed by the detector 75% of the time. Therefore, rather than adjusting the selection to
²⁰⁰ require exactly 2 b-tagged jets, and losing more than half of the signal events, a neural network is
²⁰¹ used to predict which pair of jets is most likely to correspond to truth b-jets.

²⁰² Once the network is trained, all possible pairings of jets are fed into the model, and the pair of jets
²⁰³ with the highest output score are taken to be b-jets in successive steps of the analysis.

²⁰⁴ **5.2.1 2lSS Channel**

²⁰⁵ For the 2lSS channel, the input features shown in table 3 are used for training. Here j_0 and j_1 are
²⁰⁶ the two jet candidates, while l_0 and l_1 are the two leptons in the event, both ordered by p_T . jet
²⁰⁷ DL1r is an integer corresponding to the calibrated b-tagging working points reached by each jet,

208 where 5 represents the tightest working point and 1 represents the loosest. The variables nJets
 209 DL1r 60% and nJets DL1r 85% represent the number of jets in the event passing the 60% and
 210 85% b-tag working points, respectively.

jet p_T 0	jet p_T 1	Lepton p_T 0
Lepton p_T 1	jet η 0	jet η 1
$\Delta R(j_0)(j_1)$	$M(j_0 j_1)$	$\Delta R(l_0)(j_0)$
$\Delta R(l_0)(j_1)$	$\Delta R(l_1)(j_0)$	$\Delta R(l_1)(j_1)$
$M(l_0 j_0)$	$M(l_0 j_1)$	$M(l_1 j_0)$
$M(l_1 j_1)$	jet DL1r 0	jet DL1r 1
nJets OR DL1r 85	nJets OR DL1r 60	$\Delta R(j_0 l_0)(j_1 l_1)$
$\Delta R(j_0 l_1)(j_1 l_0)$	$p_T(j_0 j_1 l_0 l_1 E_T^{\text{miss}})$	$M(j_0 j_1 l_0 l_1 E_T^{\text{miss}})$
$\Delta\phi(j_0)(E_T^{\text{miss}})$	$\Delta\phi(j_1)(E_T^{\text{miss}})$	HT jets
nJets	E_T^{miss}	

Table 3: Input features used in the b-jet identification algorithm for the 2lSS channel

211 As there are far more incorrect combinations than correct ones, by a factor of more than 20:1, the
 212 training set is resampled to reduce the fraction of incorrect combinations. A random sample of 5
 213 million incorrect entries are used for training, along with close 1 million correct entries. 10% of
 214 the dataset is set aside for testing, leaving around 5 million datapoints for training.

215 The difference between the distributions for a few of these features for the correct (i.e. both jets
 216 are truth b-jets), and incorrect combinations are shown in figure 5.1. The correct and incorrect
 217 contributions are scaled to the same integral, so as to better demonstrate the differences in the
 218 distributions.

219 The modeling of these inputs is validated against data, with figure 5.2 showing good general
 220 agreement between data and MC. Plots for the complete list of features can found in section A.

221 Based on the results of grid search evaluation, the optimal architecture is found to include 5
 222 hidden layers with 40 nodes each. No regularizer or dropout is added to the network, as overfitting
 223 is found to not be an issue. The output score distribution as well as the ROC curve for the trained
 224 model are shown in figure 5.2.1. The model is found to identify the correct pairing of jets for
 225 73% of 2lSS signal events on test data.

226 For point of comparison, a naïve approach to identify b-jets is used as well: The two jets which
 227 pass the highest DL1r b-tag working point are assumed to be the b-jets from the top decay. In the
 228 case that multiple jets meet the same b-tag working point, the jet with higher p_T is used. This
 229 method identifies the correct jet pair 65% of the time.

230 The accuracy of the model for different values of n-bjets, compared to this naive approach, is
 231 shown in table 4.

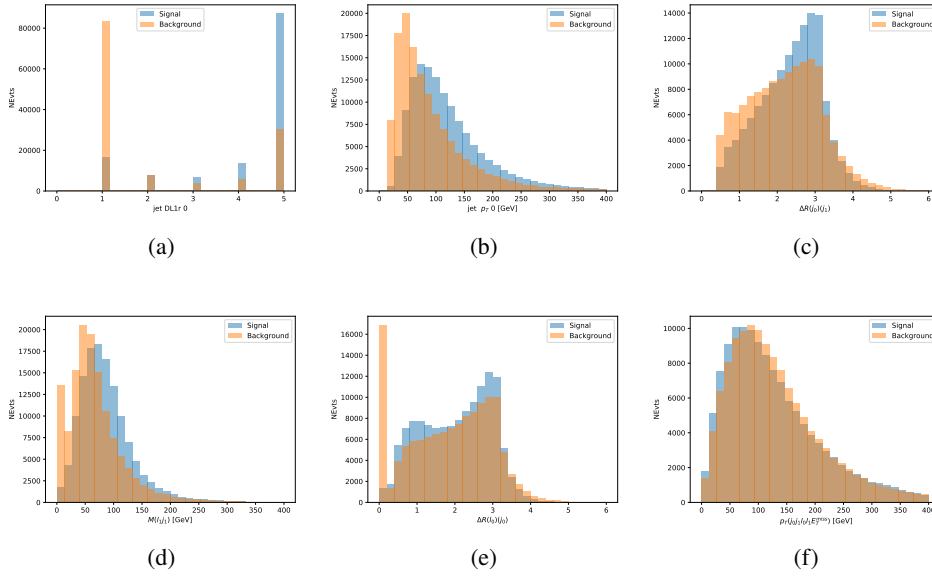


Figure 5.1: Input features for top2ISS training. The signal in blue represents events where both jet candidates are truth b-jets from top decays, and the orange is all other combinations. Each are scaled to the same number of events. (a) shows the DL1r working point of leading jet, (b) shows the p_T of the leading jet, (c) shows the ΔR of the two jets, (d) the invariant mass of lepton 1 and jet 1, (e) the ΔR of lepton 0 and jet 0, and (f) the p_T of both jets, both leptons, and the E_T^{miss} .

Table 4: Accuracy of the NN in identifying b-jets from tops in 2lSS events for, compared to the accuracy of taking the two highest b-tagged jets.

b-jet Selection	Neural Network	Naive
1 b-jet	58.6%	42.1%
2 b-jets	88.4%	87.1%
$>=3$ b-jets	61.7%	53.3%
Overall	73.9% %	67.2%

5.2.2 3l Channel

The input features used in the 3l channel are listed in table 5, with the same naming convention as the 2lSS channel.

A few of these features are shown in figure 5.4, comparing the distributions for correct and incorrect combinations of jets.

The modeling of these inputs is validated against data, with figure 5.5 showing good general agreement between data and MC. Plots for the complete list of features can be found in section A.

Again, the dataset is downsized to reduce the ratio of correct and incorrect combination from 20:1,

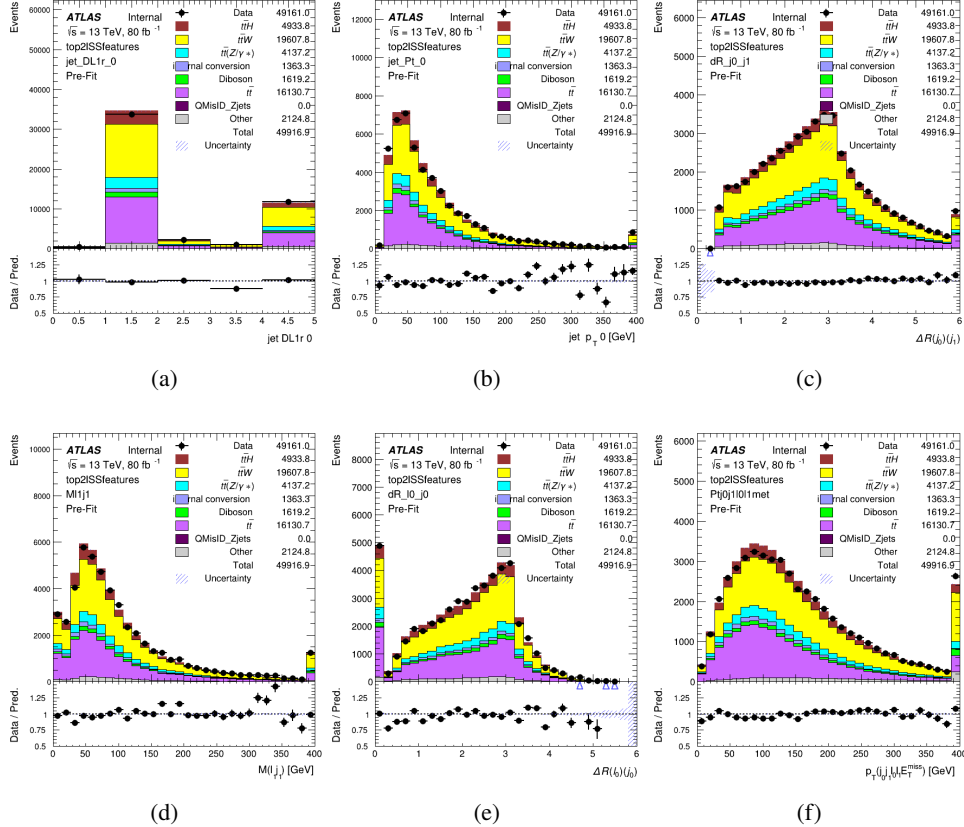


Figure 5.2: Data/MC comparisons of input features for top2lSS training for 80 fb^{-1} of data. (a) shows the DL1r working point of leading jet, (b) shows the p_T of the leading jet, (c) shows the ΔR of the two jets, (d) the invariant mass of lepton 1 and jet 1, (e) the ΔR of lepton 0 and jet 0, and (f) the p_T of both jets, both leptons, and the E_T^{miss} .

to 5:1. Around 7 million events are used for training, with 10% set aside for testing. Based on the results of grid search evaluation, the optimal architecture is found to include 5 hidden layers with 60 nodes each. The output score distribution as well as the ROC curve for the trained model are shown in figure 5.2.2.

This procedure is found to identify the correct pairing of jets for nearly 80% of 31 signal events. The accuracy of the model is summarized in table 6.

5.3 Higgs Reconstruction

Techniques similar to the b-jet identification algorithms are employed to select the decay products of the Higgs: kinematics of all possible combinations of reconstructed objects are fed into a neural network to determine which of those is most mostly to be the decay products of the Higgs.

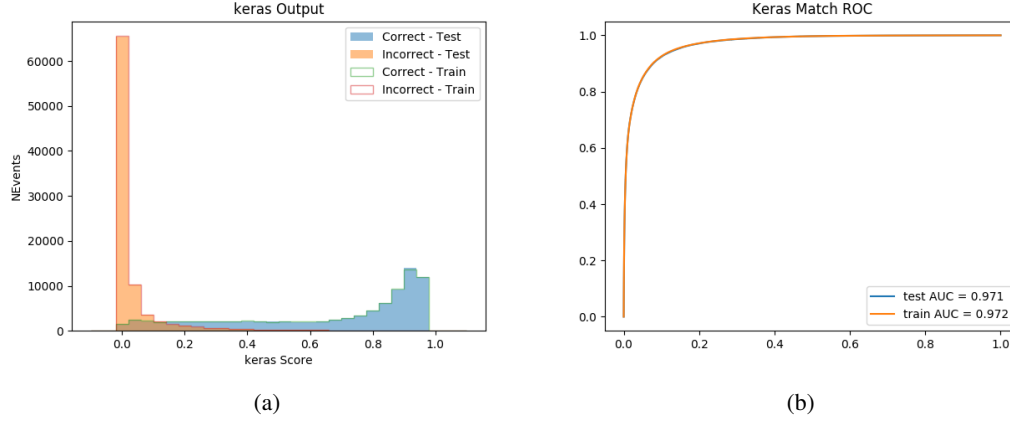


Figure 5.3: Results of the b-jet identification algorithm for the 2lSS channel, showing (a) the output score of the NN for correct and incorrect combinations of jets. (b) the ROC curve of the output, showing background rejection as a function of signal efficiency

jet p_T 0	jet p_T 1	jet η 0
jet η 1	Lepton p_T 0	Lepton p_T 1
Lepton p_T 2	$\Delta R(j_0)(j_1)$	$M(j_0 j_1)$
$\Delta R(l_0)(j_0)$	$\Delta R(l_1)(j_0)$	$\Delta R(l_2)(j_0)$
$\Delta R(l_0)(j_1)$	$\Delta R(l_1)(j_1)$	$\Delta R(l_2)(j_1)$
$M(l_0 j_0)$	$M(l_1 j_0)$	$M(l_2 j_0)$
$M(l_0 j_1)$	$M(l_1 j_1)$	$M(l_2 j_1)$
$\Delta R(j_0 l_0)(j_1 l_1)$	$\Delta R(j_0 l_0)(j_1 l_2)$	$\Delta R(j_0 l_1)(j_1 l_0)$
$\Delta R(j_0 l_2)(j_1 l_0)$	jet DL1r 0	jet DL1r 1
$p_T(j_0 j_1 l_0 l_1 l_2 E_T^{\text{miss}})$	$M(t_j j_1 l_0 l_1 l_2 E_T^{\text{miss}})$	$\Delta\phi(j_0)(E_T^{\text{miss}})$
$\Delta\phi(j_1)(E_T^{\text{miss}})$	HT Lepton	HT jets
nJets	E_T^{miss}	nJets OR DL1r 85
nJets OR DL1r 60		

Table 5: Input features for the b-jet identification algorithm in the 3l channel.

Table 6: Accuracy of the NN in identifying b-jets from tops, compared to the naive method of taking the highest b-tagged jets.

	NN	Naive
1 b-jet	69.0%	48.9%
2 b-jets	89.6%	88.3%
≥ 3 b-jets	55.7%	52.3%
Overall	79.8%	70.2%

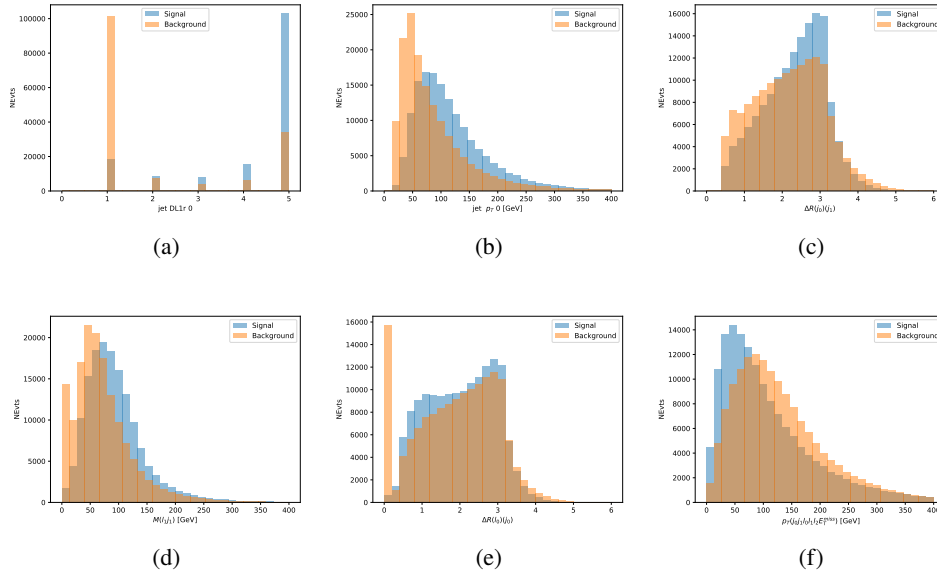


Figure 5.4: Input features for top3l training. The signal in blue represents events where both jet candidates are truth b-jets from top decays, and the orange is all other combinations. Scaled to the same number of events.

Again separate models are used for the 2ISS and 3l channels, while the 3l channel has now been split into two: $t\bar{t}H$ events with three leptons in the final state include both instances where the Higgs decays into a lepton (and a neutrino) and a pair of jets, and instances where the Higgs decays to two leptons.

3l events are therefore categorized as either semi-leptonic (3IS) or fully-leptonic (3IF). In the semi-leptonic case the reconstructed decay products consist of two jets and a single leptons. For the fully-leptonic case, the decay products include 2 of the three leptons associated with the event. For training the models, events are separated into these two categories using truth level information. A separate MVA, described in section 5.5, is used to make this distinction at reco level and determine which model to use.

For all channels, the models described in section 5.2 are used to identify b-jet candidates, whose kinematics are used to identify the Higgs decay products. These jets are not considered as possible candidates for the Higgs decay, justified by the fact that these models are found to misidentify jets from the Higgs decay as jets from the top decay less than 1% of the time.

5.3.1 2ISS Channel

For the 2ISS channel, the Higgs decay products include one light lepton and two jets. The neural network is trained on the kinematics of different combinations of leptons and jets, as well as the

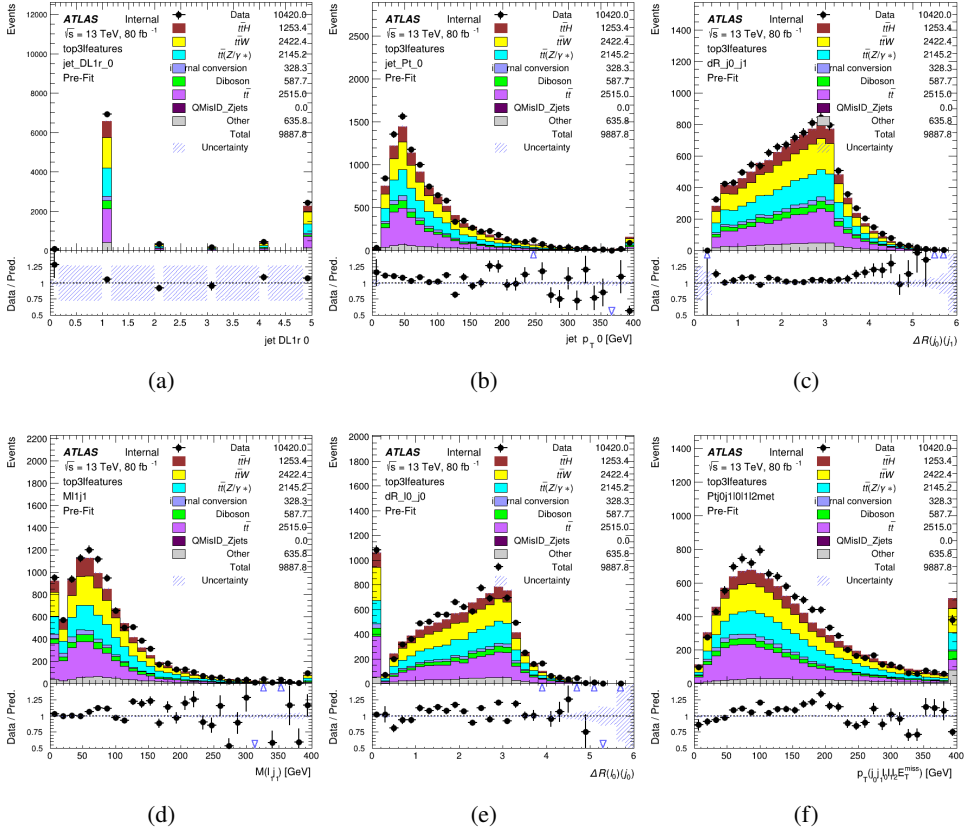


Figure 5.5: Data/MC comparisons of input features for top3l training for 80 fb^{-1} of data.

267 b-jets identified in section 5.2, with the specific input features listed in table ??.

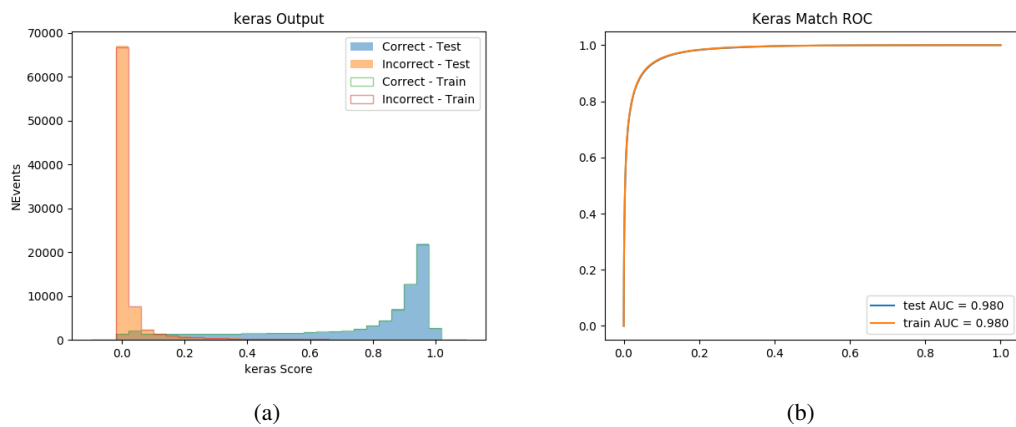


Figure 5.6: Results of the b-jet identification algorithm for the 3l channel, showing (a) the output score of the NN for correct and incorrect combinations of jets. (b) the ROC curve of the output, showing background rejection as a function of signal efficiency

Lepton p_T H	Lepton p_T T	jet p_T 0
jet p_T 1	top p_T 0	top p_T 1
top η 0	top η 1	jet η 0
jet η 1	jet Phi 0	jet Phi 1
Lepton η H	Lepton η T	$\Delta R(j_0)(j_1)$
$\Delta R(l_H)(j_0)$	$\Delta R(l_H)(j_1)$	$M(j_0 j_1)$
$M(l_H j_0)$	$M(l_H j_1)$	$\Delta R(l_H)(b_0)$
$\Delta R(l_H)(b_1)$	$\Delta R(l_T)(b_0)$	$\Delta R(l_T)(b_1)$
$\Delta R(j_0 j_1)(l_H)$	$\Delta R(j_0 j_1)(l_T)$	$\Delta R(j_0 j_1)(b_0)$
$\Delta R(j_0 j_1)(b_1)$	$\Delta R(j_0)(b_0)$	$\Delta R(j_0)(b_1)$
$\Delta R(j_1)(b_0)$	$\Delta R(j_1)(b_1)$	$M(j_0 j_1 l_H)$
$p_T(j_0 j_1 l_H l_T b_0 b_1 E_T^{\text{miss}})$	topScore	E_T^{miss}
nJets	HT jets	

Table 7: Input features

268 Here j_0 and j_1 , and l_H are the jet and lepton decay candidates, respectively. The other lepton in
 269 the event is labeled l_T , as it is assumed to have come from the decay of one of the top quarks. b_0
 270 and b_1 are the two b-jets identified by the b-jet identification algorithm. The b-jet Reco Score is
 271 the output of the b-jet reconstruction algorithm.

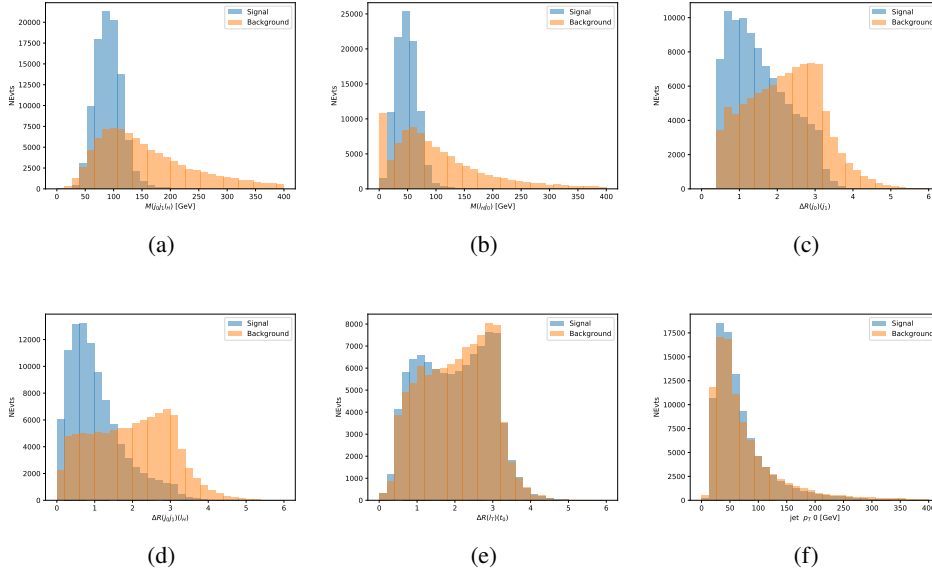


Figure 5.7: Input features for higgs2lSS training. The signal in blue represents events where both jet candidates are truth b-jets from top decays, and the orange is all other combinations. Scaled to the same number of events.

272 The modeling of these inputs is validated against data, with figure 5.2 showing good general
 273 agreement between data and MC. Plots for the complete list of features can found in section A.

274 A neural network consisting of 7 hidden layers with 60 nodes each is trained on around 2 million
 275 events, with an additional 200,000 reserved for testing the model. In order to compensate for
 276 large number of incorrect combinations, these have been downsampled such that the correct
 277 combinations represent over 10% of the training set. The output of the NN is summarized in
 278 figure 5.3.1.

279 The neural network identifies the correct combination 55% of the time. It identifies the correct
 280 lepton 85% of the time, and selects the correct lepton and at least one of the correct jets 81% of
 281 the time.

282 5.3.2 3l Semi-leptonic Channel

283 For 3l $t\bar{t}H$ where the Higgs decay semi-leptonically, the decay products include one of the three
 284 leptons and two jets. In this case, the other two leptons originated from the decay of the tops,

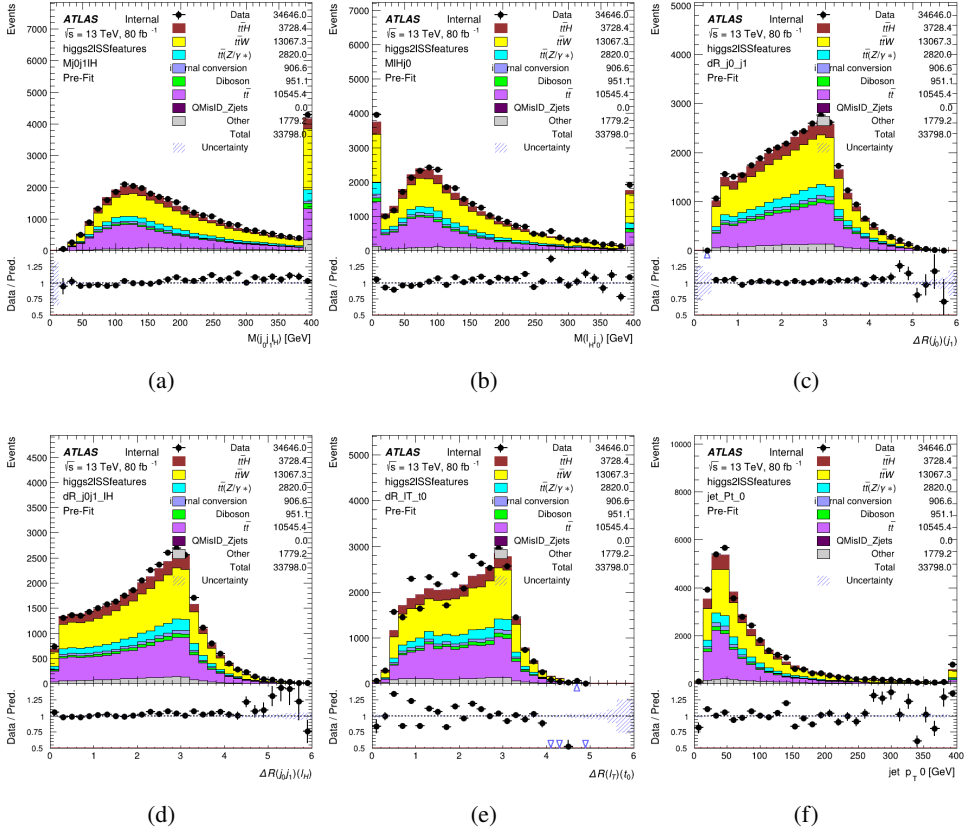


Figure 5.8: Data/MC comparisons of input features for higgs2lSS training for 80 fb^{-1} of data.

meaning the opposite-sign (OS) lepton cannot have come from the Higgs. This leaves only the two same-sign (SS) leptons as possible Higgs decay products.

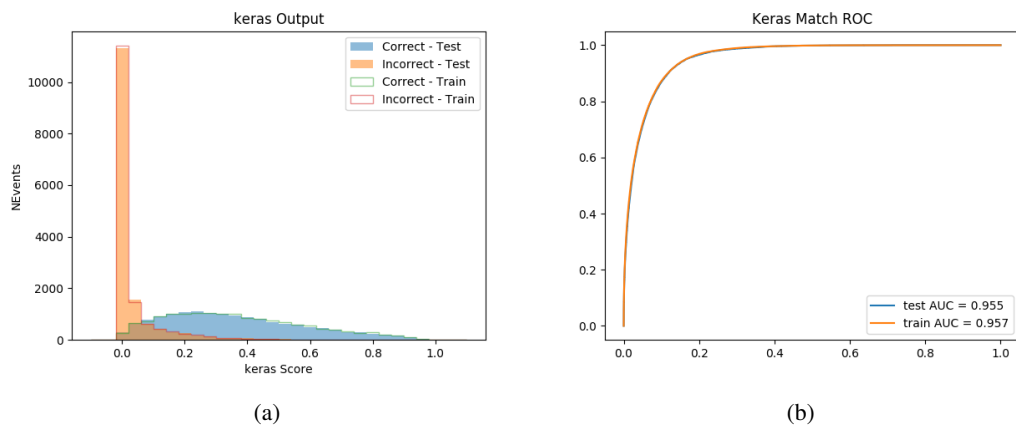


Figure 5.9: Result of the Higgs reconstruction algorithm in the 2ISS channel, showing (a) the output score of the NN for correct and incorrect combinations of jets scaled to an equal number of events, and (b) the ROC curve of the output, showing background rejection as a function of signal efficiency

Lepton $p_T H$	Lepton $p_T T_0$	Lepton $p_T T_1$
jet $p_T 0$	jet $p_T 1$	top $p_T 0$
top $p_T 1$	jet $\eta 0$	jet $\eta 1$
jet $\phi 0$	jet $\phi 1$	$\Delta R(j_0)(j_1)$
$M(j_0 j_1)$	$\Delta R(l_H)(j_0)$	$\Delta R(l_H)(j_1)$
$\Delta R(j_0 j_1)(l_H)$	$\Delta R(j_0 j_1)(l_{T_0})$	$\Delta R(l_{T_0})(l_{T_1})$
$\Delta R(l_H)(l_{T_1})$	$M(j_0 j_1 l_{T_0})$	$M(j_0 j_1 l_{T_1})$
$M(j_0 j_1 l_H)$	$\Delta R(j_0 j_1 l_H)(l_{T_0})$	$\Delta R(j_0 j_1 l_H)(l_{T_1})$
$\Delta\phi(j_0 j_1 l_H)(E_T^{\text{miss}})$	$p_T(j_0 j_1 l_H l_{T_0} l_{T_1} b_0 b_1 E_T^{\text{miss}})$	$M(j_0 j_1 b_0)$
$M(j_0 j_1 b_1)$	$\Delta R(l_{T_0})(b_0)$	$\Delta R(l_{T_0})(b_1)$
$\Delta R(l_{T_1})(b_0)$	$\Delta R(l_{T_1})(b_1)$	$\Delta R(j_0)(b_0)$
$\Delta R(j_0)(b_1)$	$\Delta R(j_1)(b_0)$	$\Delta R(j_1)(b_1)$
topScore	MET	HT jets
nJets		

Table 8: Input features

287 Here j_0 and j_1 , and l_H are the jet and lepton decay candidates, respectively. The other two
 288 leptons in the event are labeled as l_{T0} and l_{T1} . b_0 and b_1 are the two b-jets identified by the
 289 b-jet identification algorithm. The b-jet Reco Score is the output of the Higgs reconstruction
 290 algorithm.

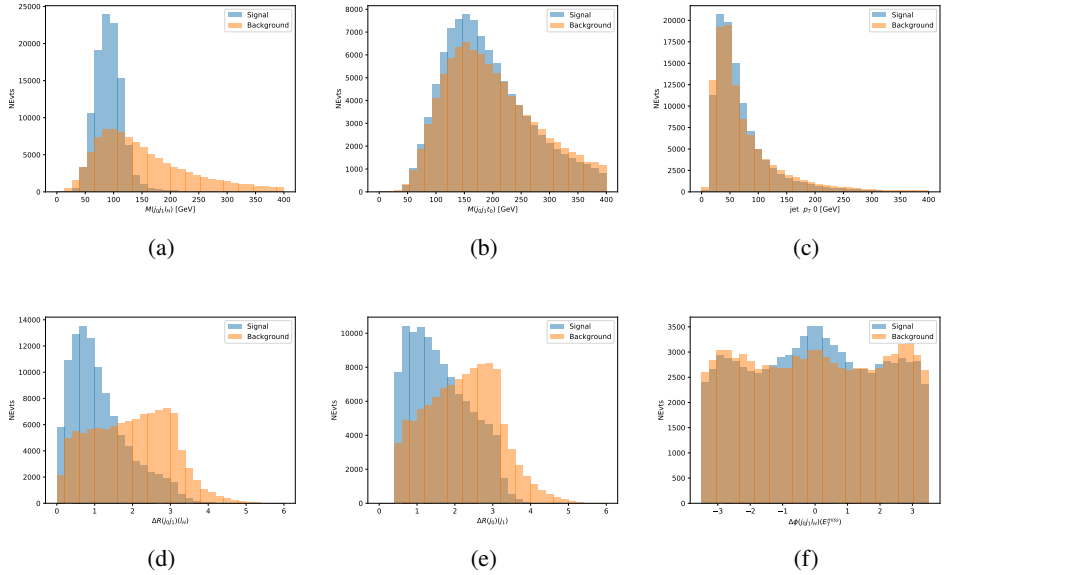


Figure 5.10: Input features for higgs3lS training. The signal in blue represents events where both jet candidates are truth b-jets from top decays, and the orange is all other combinations. Scaled to the same number of events.

291 The modeling of these inputs is validated against data, with figure 5.11 showing good general
 292 agreement between data and MC. Plots for the complete list of features can found in appendix
 293 A.1.

294 A neural network of 7 hidden layers with 70 nodes each is trained on 1.8 million events. Once
 295 again, incorrect combinations are downsampled, such that the correct combinations are around
 296 10% of the training set. 10% of the dataset is reserved for testing. The output of the NN is
 297 summarized in figure 5.3.2.

298 The neural network identifies the correct combination 64% of the time. It identifies the correct
 299 lepton 85% of the time, and selects the correct lepton and at least one of the correct jets 83% of
 300 the time.

301 5.3.3 3l Fully-leptonic Channel

302 In the fully-leptonic 3l case, the goal is identify which two of the three leptons originated from
 303 the Higgs decay. Since one of these two must be the OS lepton, this problem is reduced to

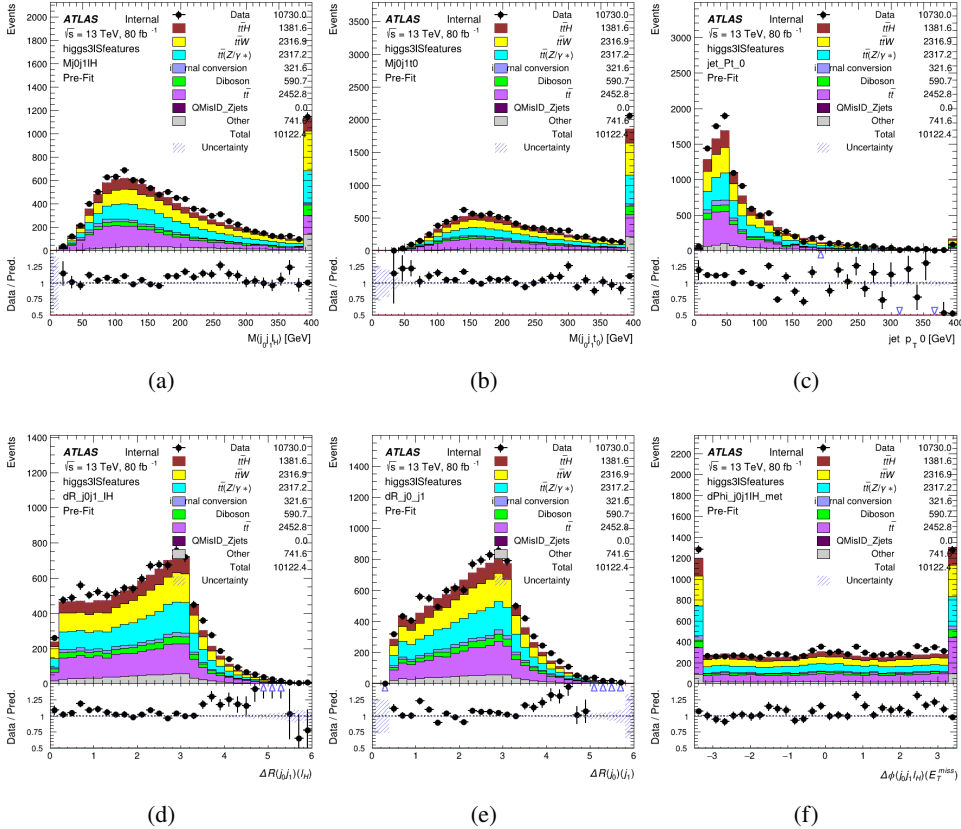


Figure 5.11: Data/MC comparisons of input features for higgs3IS training for 80 fb^{-1} of data.

determining which of the two SS leptons originated from the Higgs. The kinematics of both possibilities are used for training, one where the SS lepton from the Higgs is correctly labeled, and one where it is not.

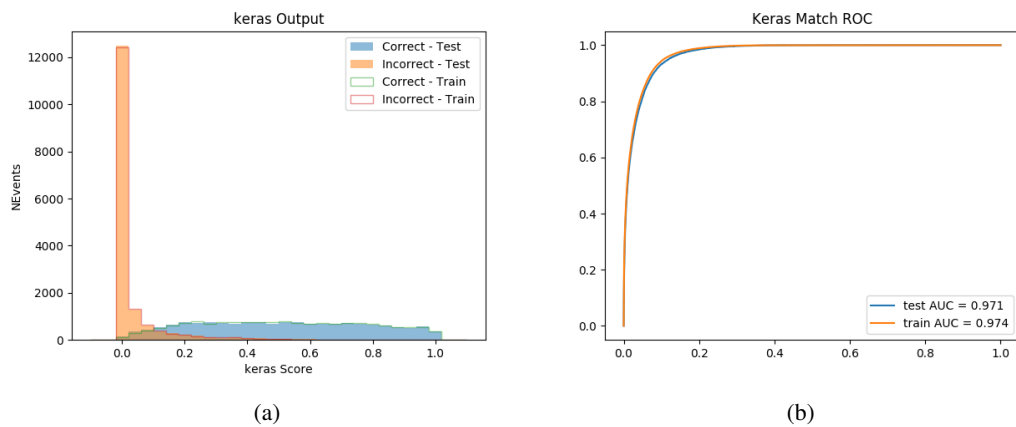


Figure 5.12: Results of the Higgs reconstruction algorithm in the 3lS channel, showing (a) the output score of the NN for correct and incorrect combinations of jets, scaled to an equal number of entries., (b) the ROC curve of the output, showing background rejection as a function of signal efficiency

Lepton $p_T H_1$	Lepton $p_T H_0$	Lepton $p_T T$
top $p_T 0$	top $p_T 1$	$\Delta\phi(l_{H_1})(E_T^{\text{miss}})$
$\Delta\phi(l_T)(E_T^{\text{miss}})$	$M(l_{H_0}l_{H_1})$	$M(l_{H_1}l_T)$
$M(l_{H_0}l_T)$	$\Delta R(l_{H_0})(l_{H_1})$	$\Delta R(l_{H_1})(l_T)$
$\Delta R(l_{H_0})(l_T)$	$\Delta R(l_{H_0}l_{H_1})(l_T)$	$\Delta R(l_{H_0}l_T)(l_{H_1})$
$\Delta R(l_{H_0}l_{H_1})(b_0)$	$\Delta R(l_{H_0}l_{H_1})(b_1)$	$\Delta R(l_{H_0}b_0)$
$M(l_{H_0}b_0)$	$\Delta R(l_{H_0}b_1)$	$M(l_{H_0}b_1)$
$\Delta R(l_{H_1}b_0)$	$M(l_{H_1}b_0)$	$\Delta R(l_{H_1}b_1)$
$M(l_{H_1}b_1)$	E_T^{miss}	topScore

Table 9: Input features

307 Here l_{H0} and l_{H1} are the Higgs decay candidates. The other lepton in the event is labeled l_T . b_0
 308 and b_1 are the two b-jets identified by the b-jet identification algorithm. The b-jet Reco Score is
 309 the output of the Higgs reconstruction algorithm.

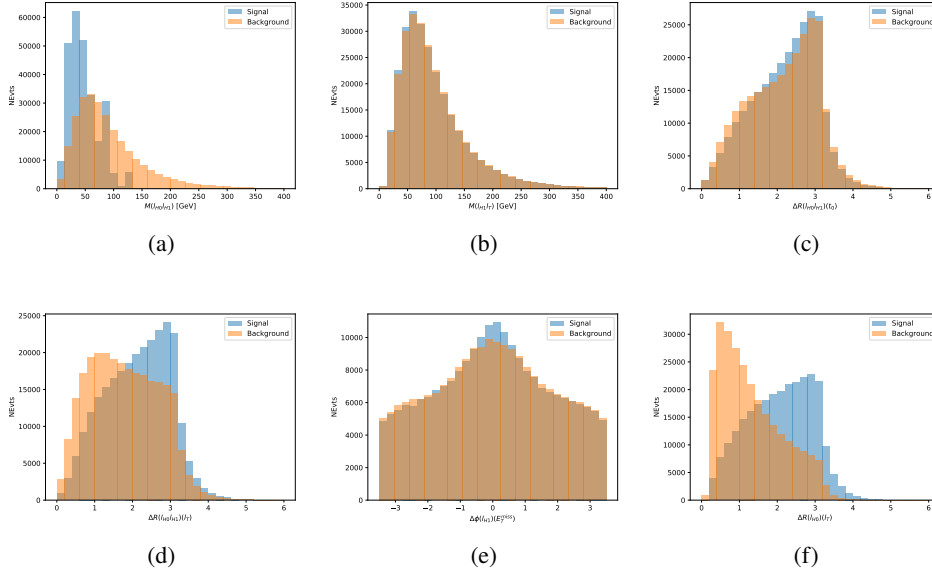


Figure 5.13: Input features for higgs3lF training. The signal in blue represents events where both jet candidates are truth b-jets from top decays, and the orange is all other combinations. Scaled to the same number of events.

310 The modeling of these inputs is validated against data, with figure 5.14 showing good general
 311 agreement between data and MC. Plots for the complete list of features can found in section A.
 312 A neural network consisting of 5 nodes and 60 hidden units is trained on 800,000 events, with
 313 10% of the dataset reserved for testing. The output of the model is summarized in figure 5.3.3.
 314 The correct lepton is identified by the model for 80% of events in the testing data set.

315 5.4 p_T Prediction

316 Once the most probable decay products have been identified, their kinematics are used as inputs
 317 to a regression model which attempts to predict the momentum of the Higgs Boson. Once again,
 318 a DNN is used. Input variables representing the b-jets and leptons not from the Higgs decay
 319 are included as well, as these are found to improve performance. The truth p_T of the Higgs,
 320 as predicted by MC, are used as labels. Separate models are built for each channel - 2lSS, 3l
 321 Semi-leptonic and 3l Fully-leptonic.

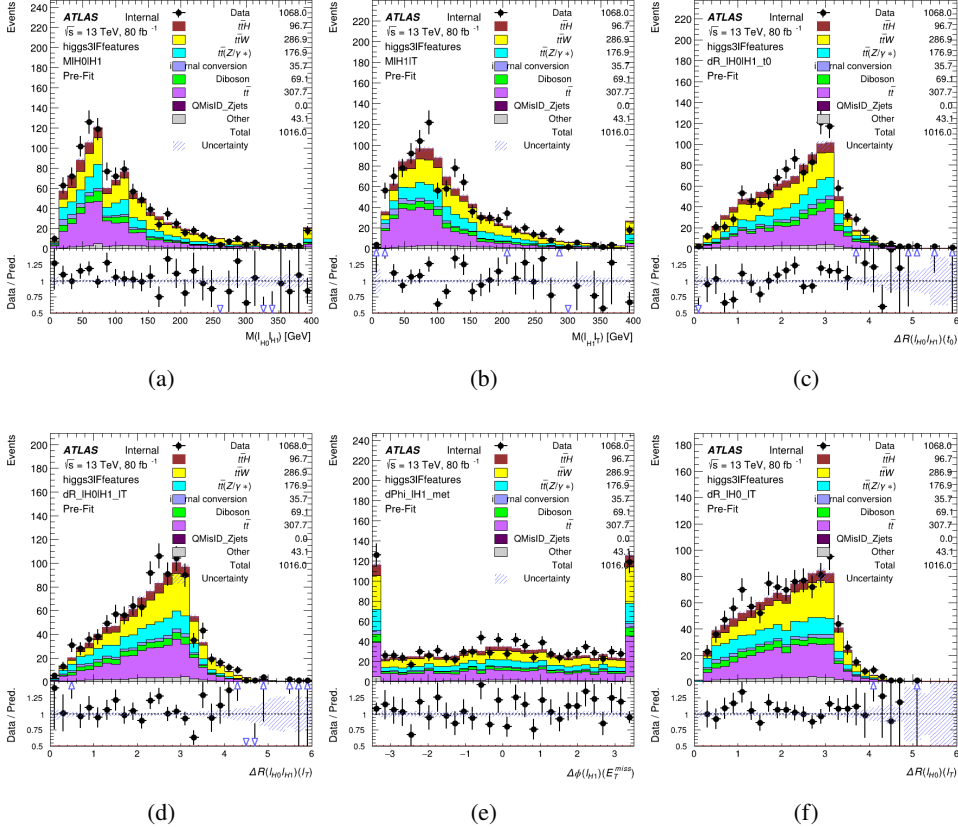


Figure 5.14: Data/MC comparisons of input features for higgs3IF training for 80 fb^{-1} of data.

As a two-bin fit is targeted for the final result, some metrics evaluating the performance of the models aim to show how well it distinguished between "high p_T " and "low p_T " events. A cutoff point of 150 GeV is used to define these two categories.

Because the analysis uses a two bin fit of the Higgs p_T , the momentum reconstruction could be treated as a binary classification problem, rather than a regression problem. This approach is explored in detail in section A.4, and is found not to provide any significant increase in sensitivity. The regression approach is used because it provides more flexibility for future analyses, as it is independent of the cutoff between high and low p_T , as well as the number of bins. Further, a regression allows the output of the neural network to be more clearly understood, as it can be directly compared to a physics observable.

5.4.1 2ISS Channel

The input variables listed in table ?? are used to predict the Higgs p_T in the 2ISS channel. Here j_0 and j_1 are the two jets identified as Higgs decay products. The lepton identified as originating

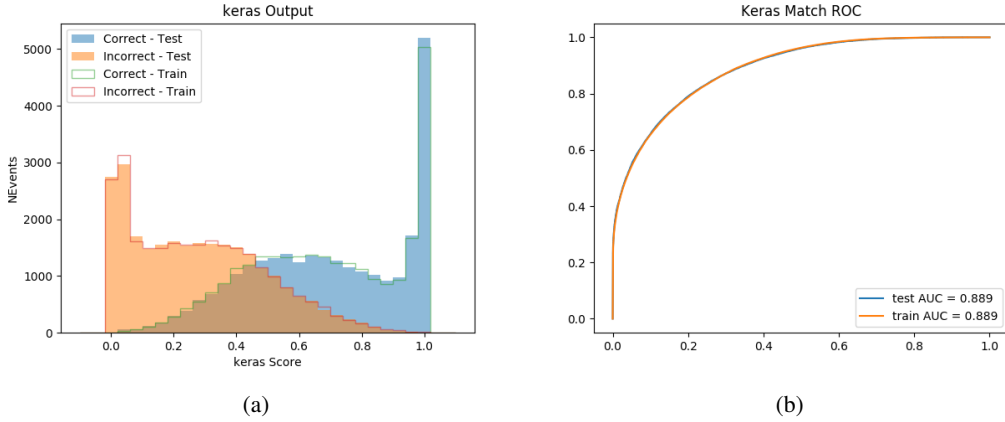


Figure 5.15: (a) the output score of the NN for correct and incorrect combinations of jets. (a) the ROC curve of the output, showing background rejection as a function of signal efficiency

335 from the Higgs is labeled l_H , while the other lepton is labeled l_T , as it is assumed to have come
 336 from the decay of one of the top quarks. b_0 and b_1 are the two b-jets identified by the b-jet
 337 identification algorithm. The Higgs Reco Score and b-jet Reco Score are the outputs of the Higgs
 338 reconstruction algorithm, and the b-jet identification algorithm, respectively.

HT	$M(j_0 j_1)$	$M(j_0 j_1 l_H)$
$M(l_H j_0)$	$M(l_H j_1)$	$(p_T)(\min \Delta R(t l_T)) [GeV]$
$p_T(j_0 j_1 l_H)$	$\Delta\phi(j_0 j_1 l_H)(E_T^{\text{miss}})$	$\Delta R(j_0)(j_1)$
$\Delta R(j_0 j_1)(l_H)$	$\Delta R(j_0 j_1 l_H)(l_T)$	$\Delta R(j_0 j_1 l_H)(b_0)$
$\Delta R(j_0 j_1 l_H)(b_1)$	$\Delta R(l_H)(j_0)$	$\Delta R(l_H)(b_0)$
$\Delta R(l_H)(b_1)$	$\Delta R(l_T)(b_0)$	$\Delta R(l_T)(b_1)$
$\Delta R(b_0)(b_1)$	Higgs Reco Score	jet η 0
jet η 1	jet Phi 0	jet Phi 1
jet p_T 0	jet p_T 1	Lepton η H
Lepton ϕ H	Lepton p_T H	Lepton p_T T
E_T^{miss}	nJets	b-jet Reco Score
b-jet p_T 0	b-jet p_T 1	

Table 10: Input features for reconstructing the Higgs p_T spectrum for 2lSS events

339 The optimal neural network architecture for this channel is found to consist of 7 hidden layers with
 340 60 nodes each. The input data set includes 1.2 million events, 10% of which is used for testing,
 341 the other 90% for training. Training is found to converge after around 150 epochs.

342 To evaluate the performance of the model, the predicted p_T spectrum is compared to the truth
 343 Higgs p_T in figure 5.16. In order to visualize the model performance more clearly, in (a) of that
 344 figure, the color of each point is determined by Kernel Density Estimation (KDE). The color
 345 shown represents the logarithm of the output from KDE, to counteract the large number of low
 346 p_T events. For that same reason, each column of the histogram shown in (b) of figure 5.16 is
 347 normalized to unity. This plot therefore demonstrates what the model predicts for each slice of
 348 truth p_T .

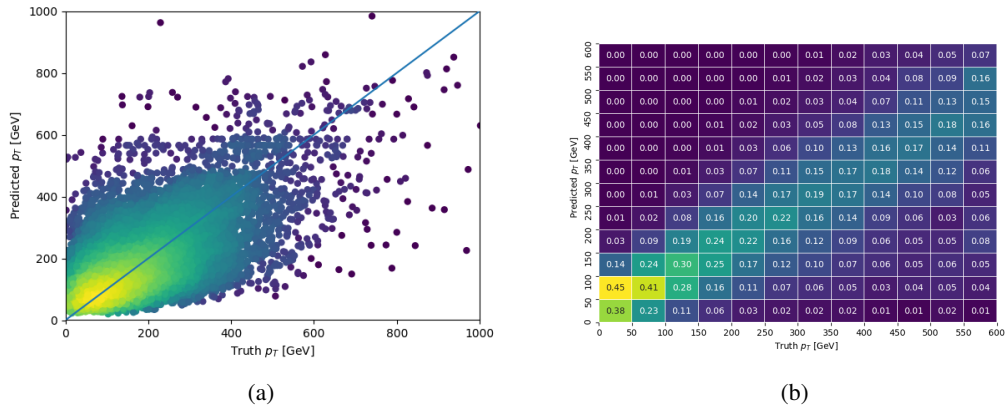


Figure 5.16: The regressed Higgs momentum spectrum as a function of the truth p_T for 2lSS $t\bar{t}H$ events in (a) a scatterplot, where the color of each point represents the log of the point density, based on Gaussian Kernel Density Estimation, and (b) a histogram where each column has been normalized to one.

349 We are also interested in how well the model distinguishes between events with $p_T < 150$ GeV
 350 and > 150 GeV. Figure 5.17 demonstrates the NN output for high and low p_T events based on this
 351 cutoff.

352 5.4.2 3l Semi-leptonic Channel

353 The following input features are used to predict the Higgs p_T for events in the 3lS channel:

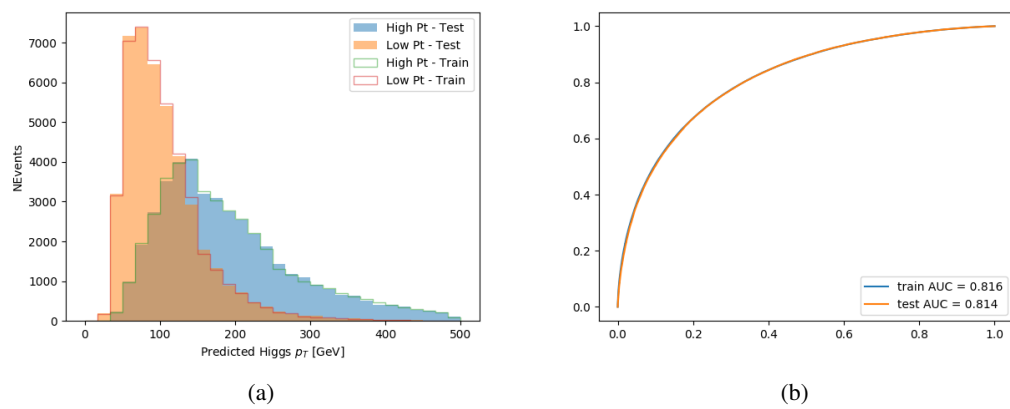


Figure 5.17: (a) shows the reconstructed Higgs p_T for 2lSS events with truth $p_T > 150$ GeV and < 150 GeV, while (b) shows the ROC curve for those two sets of events.

HT jets	MET	M(j ₀ j ₁)
M(j ₀ j ₁ l _H)	M(j ₀ j ₁ l _{T0})	M(j ₀ j ₁ l _{T1})
M(j ₀ j ₁ b ₀)	M(j ₀ j ₁ b ₁)	M(b ₀ l _{T0})
M(b ₀ l _{T1})	M(b ₁ l _{T0})	M(b ₁ l _{T1})
Δφ(j ₀ j ₁ l _H)(E _T ^{miss})	ΔR(j ₀)(j ₁)	ΔR(j ₀ j ₁)(l _H)
ΔR(j ₀ j ₁)(l _{T1})	ΔR(j ₀ j ₁)(b ₀)	ΔR(j ₀ j ₁)(b ₁)
ΔR(j ₀ j ₁ l _H)(l _{T0})	ΔR(j ₀ j ₁ l _H)(l _{T1})	ΔR(j ₀ j ₁ l _H)(b ₀)
ΔR(j ₀ j ₁ l _H)(b ₁)	ΔR(l _H)(j ₀)	ΔR(l _H)(j ₁)
ΔR(l _H)(l _{T1})	ΔR(l _{T0})(l _{T1})	ΔR(l _{T0})(b ₀)
ΔR(l _{T0})(b ₁)	ΔR(l _{T1})(b ₀)	ΔR(l _{T1})(b ₁)
higgsScore	jet η 0	jet η 1
jet φ 0	jet φ 1	jet p _T 0
jet p _T 1	Lepton η H	Lepton φ H
Lepton p _T H	Lepton p _T T0	Lepton p _T T1
nJets	topScore	b-jet p _T 0
b-jet p _T 1		

Table 11: Input features

354 Again, j_0 and j_1 are the two jets identified as Higgs decay products, ordered by p_T . The lepton
 355 identified as originating from the Higgs is labeled l_H , while the other two leptons are labeled l_{T0}
 356 and l_{T1} . b_0 and b_1 are the two b-jets identified by the b-jet identification algorithm. The Higgs
 357 Reco Score and b-jet Reco Score are the outputs of the Higgs reconstruction algorithm, and the
 358 b-jet identification algorithm, respectively.

359 The optimal neural network architecture for this channel is found to consist of 7 hidden layers
 360 with 80 nodes each. The input data set includes one million events, 10% of which is used for
 361 testing, the other 90% for training. Training is found to converge after around 150 epochs.

362 To evaluate the performance of the model, the predicted p_T spectrum is compared to the truth
 363 Higgs p_T in figure 5.18. Once again, (a) of 5.18 shows a scatterplot of predicted vs truth p_T ,
 364 where the color of each point corresponds to the log of the relative KDE at that point. Each
 365 column of the histogram in (b) is normalized to unity, to better demonstrate the output of the
 366 NN for each slice of truth p_T .

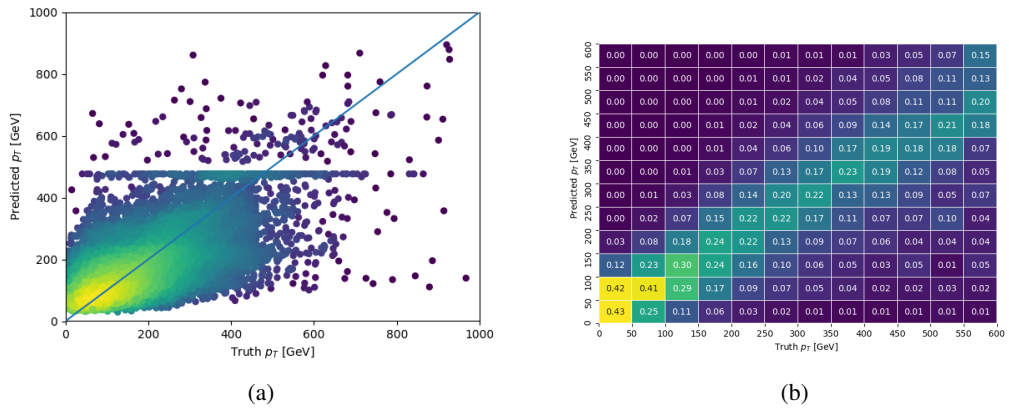


Figure 5.18:

367 Figure 5.19 shows (a) the output of the NN for events with truth p_T less than and greater than
 368 150 GeV and (b) the ROC curve demonstrating how well the NN distinguishes high and low p_T
 369 events.

370 5.4.3 3l Fully-leptonic Channel

371 The features listed in ?? are used to construct a model for predicting the Higgs p_T for 3lF events.

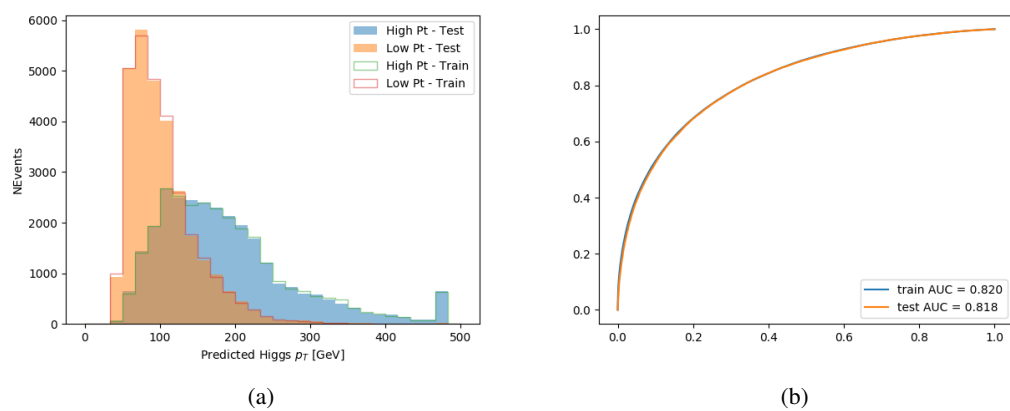


Figure 5.19:

HT	$M(l_{H0}l_{H1})$	$M(l_{H0}l_T)$
$M(l_{H0}b_0)$	$M(l_{H0}b_1)$	$M(l_{H1}l_T)$
$M(l_{H1}b_0)$	$M(l_{H1}b_1)$	$\Delta R(l_{H0})(l_{H1})$
$\Delta R(l_{H0})(l_T)$	$\Delta R(l_{H0}l_{H1})(l_T)$	$\Delta R(l_{H0}l_T)(l_{H1})$
$\Delta R(l_{H1})(l_T)$	$\Delta R(l_{H0}b_0)$	$\Delta R(l_{H0}b_1)$
$\Delta R(l_{H1}b_1)$	$\Delta R(l_{H1}b_0)$	higgsScore
Lepton η H_0	Lepton η H_1	Lepton η T
Lepton p_T H_0	Lepton p_T H_1	Lepton p_T T
E_T^{miss}	topScore	b-jet p_T 0
b-jet p_T 1		

Table 12: Input features

372 l_{H0} and l_{H1} represent the two leptons identified by the Higgs reconstruction model as originating
 373 from the Higgs, while l_T is the other lepton in the event. The Higgs Reco Score and b-jet Reco
 374 Score are the outputs of the Higgs reconstruction algorithm, and b-jet identification algorithm,
 375 respectively.

376 The optimal neural network architecture for this channel is found to consist of 5 hidden layers
 377 with 40 nodes each. The input data set includes 400,000 events, 10% of which is used for testing,
 378 the other 90% for training. Training is found to converge after around 150 epochs.

379 The predicted transverse momentum, as a function of the truth p_T , is shown in figure ??.

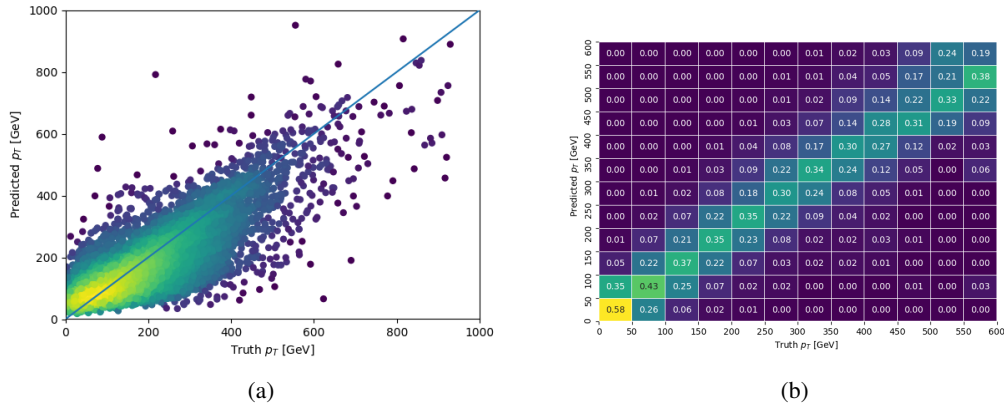


Figure 5.20:

380 When split into high and low p_T , based on a cutoff of 150 GeV, the

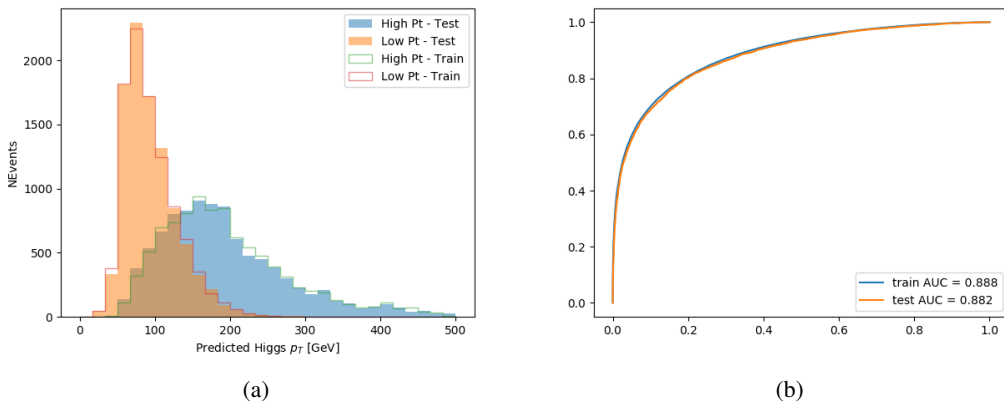


Figure 5.21:

381 5.5 3l Decay Mode

382 In the 3l channel, there are two possible ways for the Higgs to decay, both involving intermediate
383 W boson pairs: Either both W bosons decay leptonically, in which case the reconstructed decay
384 consists of two leptons (referred as the fully-leptonic 3l channel), or one W decays leptonically
385 and the other hadronically, giving two jets and one lepton in the final state (referred to as the
386 semi-leptonic 3l channel). In order to accurately reconstruct the Higgs, it is necessary to identify
387 which of these decays took place for each 3l event.

388 The kinematics of each event, along with the output scores of the Higgs and top reconstruction
389 algorithms, are used to distinguish these two possible decay modes. The particular inputs used
390 are listed in table ??.

HT jets	$M(l_0 t_0)$	$M(l_0 t_1)$
$M(l_1 t_0)$	$M(l_1 t_1)$	$M(l_0 l_1)$
$M(l_0 l_2)$	$M(l_1 l_2)$	$\Delta R(l_0 t_0)$
$\Delta R(l_0 t_1)$	$\Delta R(l_1 t_0)$	$\Delta R(l_1 t_1)$
$\Delta R(l l_0 1)$	$\Delta R(l l_0 2)$	$\Delta R(l l_1 2)$
Lepton η 0	Lepton η 1	Lepton η 2
Lepton ϕ 0	Lepton ϕ 1	Lepton ϕ 2
Lepton p_T 0	Lepton p_T 1	Lepton p_T 2
E_T^{miss}	nJets	nJets OR DL1r 60
nJets OR DL1r 85	score3lF	score3lS
topScore	total charge	

Table 13: Input features

391 Here l_0 is the opposite charge lepton, l_1 and l_2 are the two SS leptons order by ΔR from lepton 0.
 392 score3lF and score3lS are the outputs of the 3lS and 3lF Higgs reconstruction algorithms, while
 393 topScore is the output of the b-jet identification algorithm.

394 A neural network with 5 hidden layers, each with 50 nodes, is trained to distinguish these two
 395 decay modes. The output of the model is summarized in figure 5.22.

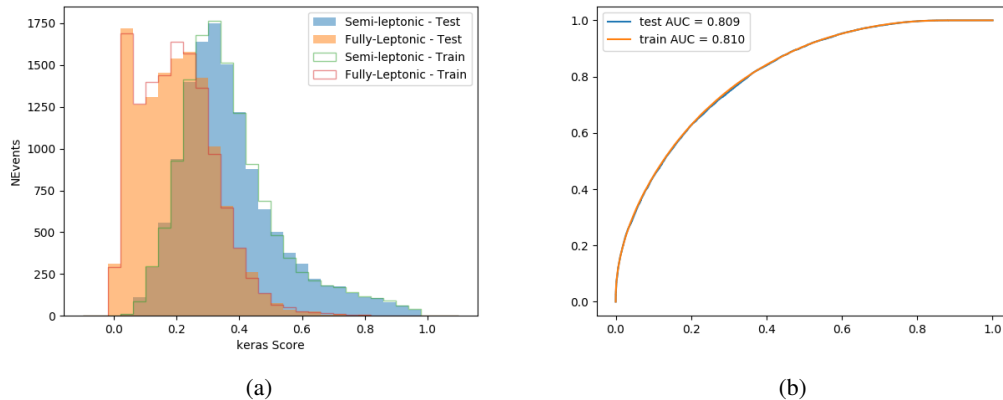


Figure 5.22:

396 A cutoff of 0.23 is determined to be optimal for separating 3lS and 3lF in the fit.

397 6 Signal Region Definitions

398 Events are divided into two channels based on the number of leptons in the final state: one with
 399 two same-sign leptons, the other with three leptons. The 3l channel includes events where both
 400 leptons originated from the Higgs boson as well as events where only one of the leptons

401 6.1 Pre-MVA Event Selection

402 A preselection is applied to define orthogonal analysis channels based on the number of leptons
 403 in each event. For the 2lSS channel, the following preselection is used:

- 404 • Two very tight, same-charge, light leptons with $p_T > 20$ GeV
- 405 • $>=4$ reconstructed jets, $>=1$ b-tagged jets
- 406 • No reconstructed tau candidates

407 For the 3l channel, the following selection is applied:

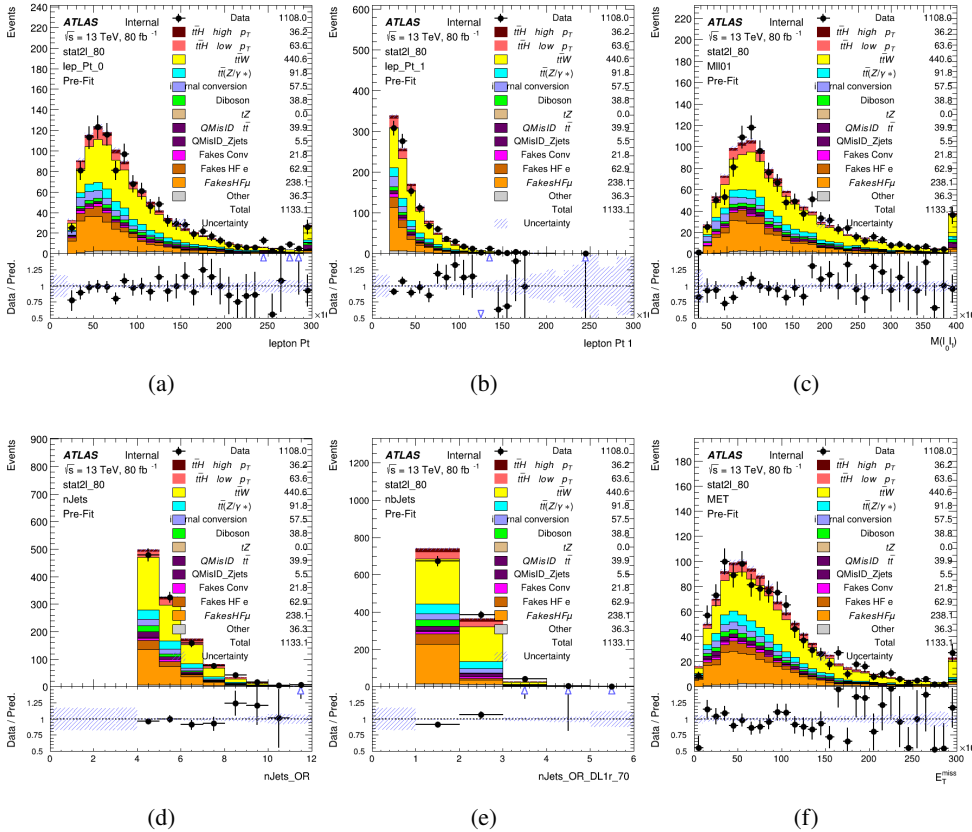


Figure 6.1:

- Three light leptons with total charge ± 1
- Same charge leptons are required to be very tight, with $p_T > 20$ GeV
- Opposite charge lepton must be loose, with $p_T > 10$ GeV
- ≥ 2 reconstructed jets, ≥ 1 b-tagged jets
- No reconstructed tau candidates
- $|M(l^+l^-) - 91.2 \text{ GeV}| > 10 \text{ GeV}$ for all opposite-charge, same-flavor lepton pairs

414 6.2 Event MVA

415 Separate multi-variate analysis techniques (MVAs) are used in order to distinguish signal events
 416 from background for each analysis channel - 2lSS, 3l semi-leptonic (3lS), and 3l fully leptonic (3lF).
 417 In particular, Boosted Decision Tree (BDT) algorithms are produced with XGBoost [[xgboost](#)]

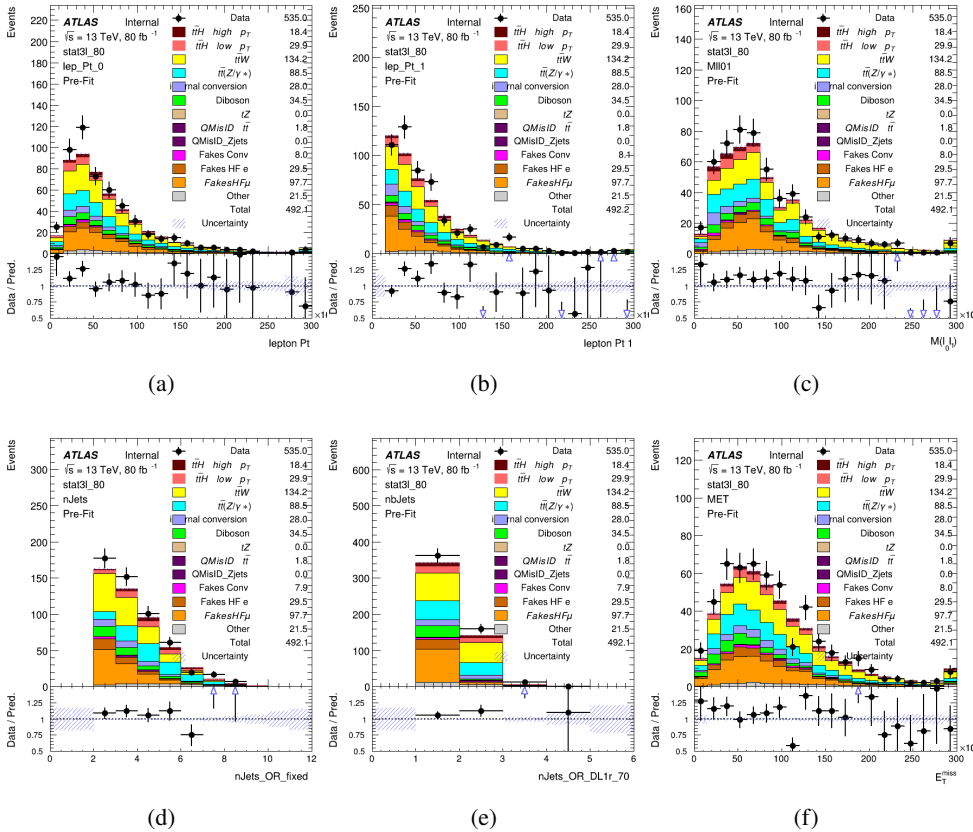


Figure 6.2:

418 are trained using the kinematics of signal and background events derived from Monte Carlo
419 simulations. Events are weighted in the BDT training by the weight of each Monte Carlo event.

420 Because the background composition differs for events with a high reconstructed Higgs p_T
421 compared to events with low reconstructed Higgs p_T , separate MVAs are produced for high and
422 low p_T regions. This is found to provide better significance than attempting to build an inclusive
423 model, as demonstrated in appendix A.2. A cutoff of 150 GeV is used. This gives a total of 6
424 background rejection MVAs - explicitly, 2lSS high p_T , 2lSS low p_T , 3lS high p_T , 3lS low p_T ,
425 3lF high p_T , and 3lF low p_T .

426 The following features are used in both the high and low p_T 2lSS BDTs:

HT	$M(\text{lep}, E_T^{\text{miss}})$	$M(l_0 l_1)$
binHiggs p_T 2lSS	$\Delta R(l_0)(l_1)$	diLepton type
higgsRecoScore	jet η 0	jet η 1
jet ϕ 0	jet ϕ 1	jet p_T 0
jet p_T 1	Lepton η 0	Lepton η 1
Lepton ϕ 0	Lepton ϕ 1	Lepton p_T 0
Lepton p_T 1	E_T^{miss}	$\min \Delta R(l_0)(\text{jet})$
$\min \Delta R(l_1)(\text{jet})$	$\min \Delta R(\text{Lepton})(\text{bjet})$	mjjMax frwdJet
nJets	nJets OR DL1r 60	nJets OR DL1r 70
nJets OR DL1r 85	signal	topRecoScore
weight		

Table 14: Input features

⁴²⁷ While for each of the 31 BDTs, the features listed below are used for training:

$M(\text{lep}, E_T^{\text{miss}})$	$M(l_0 l_1)$	$M(l_0 l_1 l_2)$
$M(l_0 l_2)$	$M(l_1 l_2)$	$\text{binHiggs } p_T \text{ 3lF}$
$\Delta R(l_0)(l_1)$	$\Delta R(l_0)(l_1)$	$\Delta R(l_0)(l_2)$
$\Delta R(l_1)(l_2)$	decayScore	higgsRecoScore3lF
higgsRecoScore3lS	$\text{jet } \eta \ 0$	$\text{jet } \eta \ 1$
$\text{jet } \phi \ 0$	$\text{jet } \phi \ 1$	$\text{jet } p_T \ 0$
$\text{jet } p_T \ 1$	$\text{Lepton } \eta \ 0$	$\text{Lepton } \eta \ 1$
$\text{Lepton } \eta \ 2$	$\text{Lepton } \phi \ 0$	$\text{Lepton } \phi \ 1$
$\text{Lepton } \phi \ 2$	$\text{Lepton } p_T \ 0$	$\text{Lepton } p_T \ 1$
$\text{Lepton } p_T \ 2$	E_T^{miss}	$\min \Delta R(l_0)(\text{jet})$
$\min \Delta R(l_1)(\text{jet})$	$\min \Delta R(l_2)(\text{jet})$	$\min \Delta R(\text{Lepton})(\text{bjet})$
$mjj\text{Max frwdJet}$	$n\text{Jets}$	$n\text{Jets OR DL1r } 60$
$n\text{Jets OR DL1r } 70$	$n\text{Jets OR DL1r } 85$	signal
topScore	triLepton type	weight

Table 15: Input features

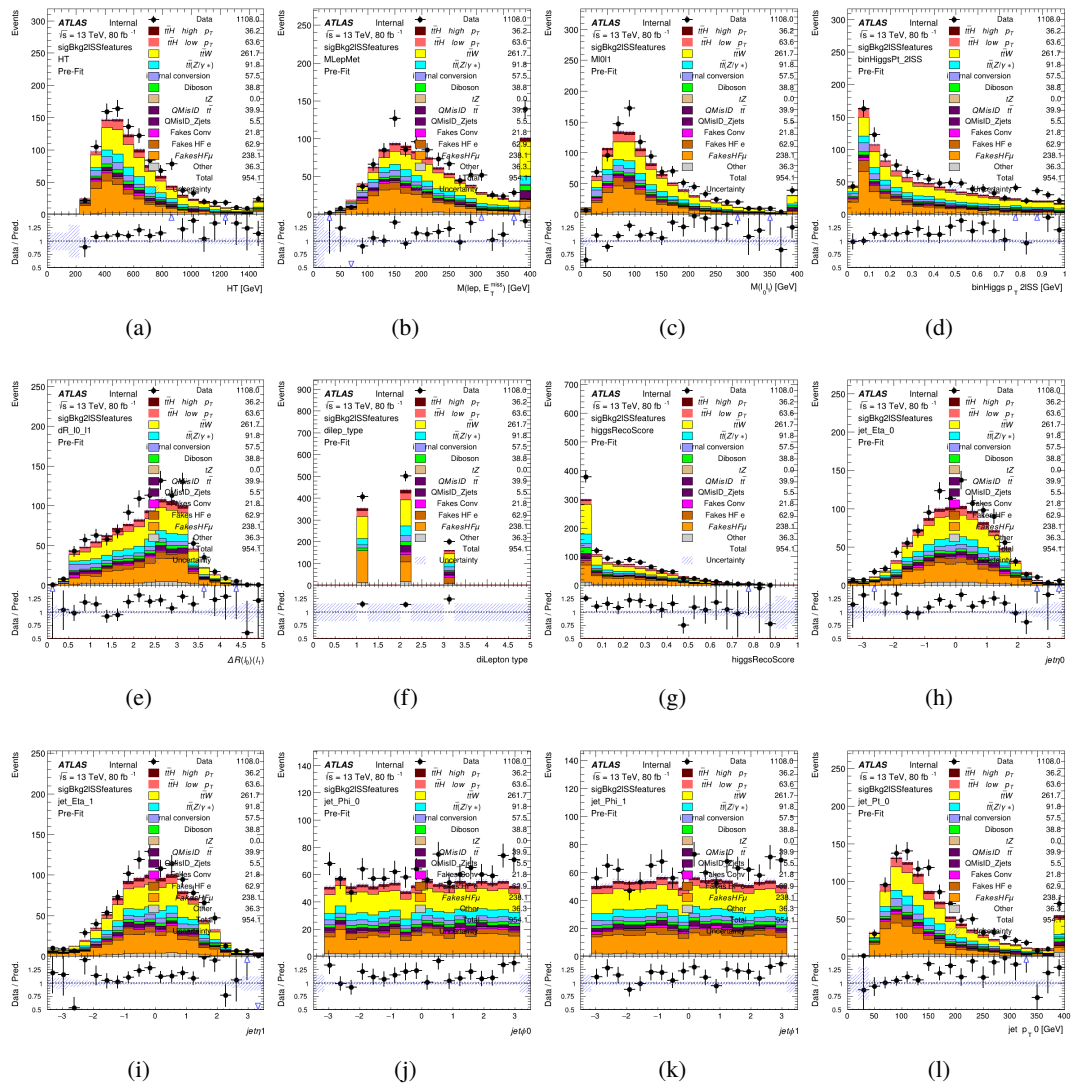


Figure 6.3:

- 428 The BDTs are produced with a maximum tree depth of 6, using AUC as the target loss function.
 429 Output distributions of each MVA are shown in figure 6.2.

430 6.3 Signal Region Definitions

- 431 Once pre-selection has been applied, channels are further refined based on the MVAs described
 432 above. The output of the model described in section 5.5 is used to separate the three channel into
 433 two - Semi-leptonic and Fully-leptonic - based on the predicted decay mode of the Higgs boson.

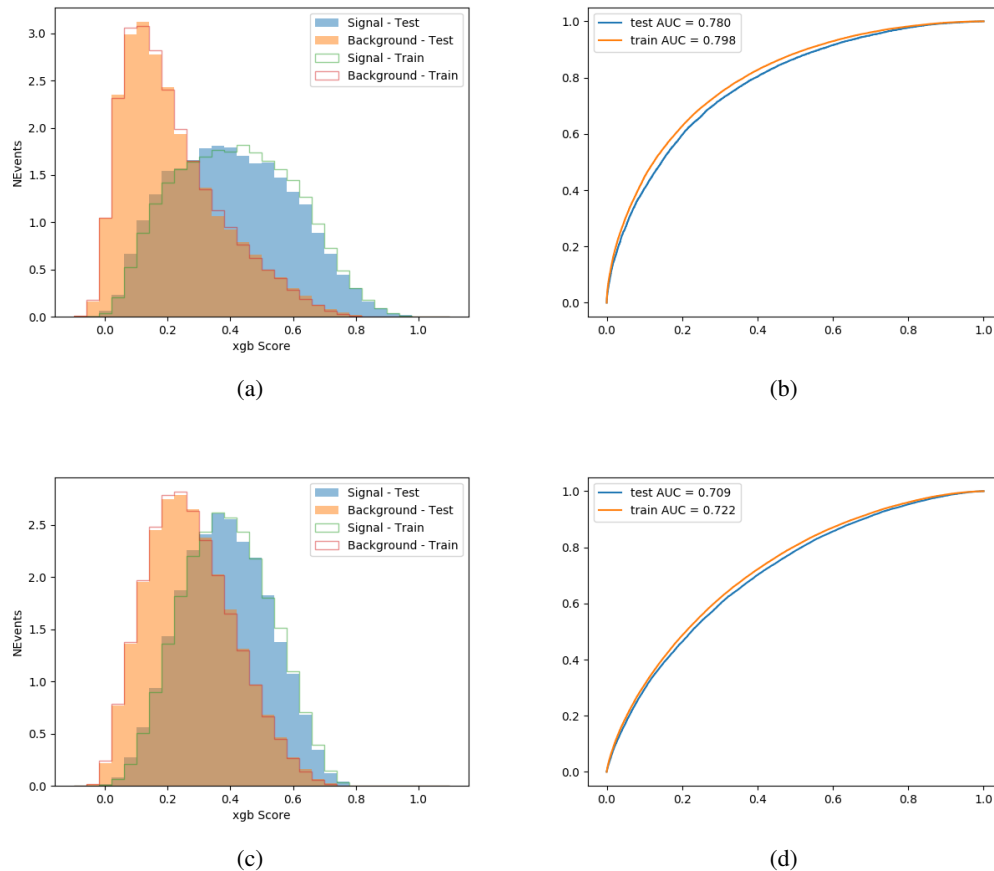


Figure 6.4:

434 For each event, depending on the channel as well as the predicted p_T of the Higgs derived from
 435 the algorithm described in section 5.4, a cut on the appropriate background rejection algorithm is
 436 applied. The specific selection used, and the event yield in each channel after this selection has
 437 been applied, is summarized below.

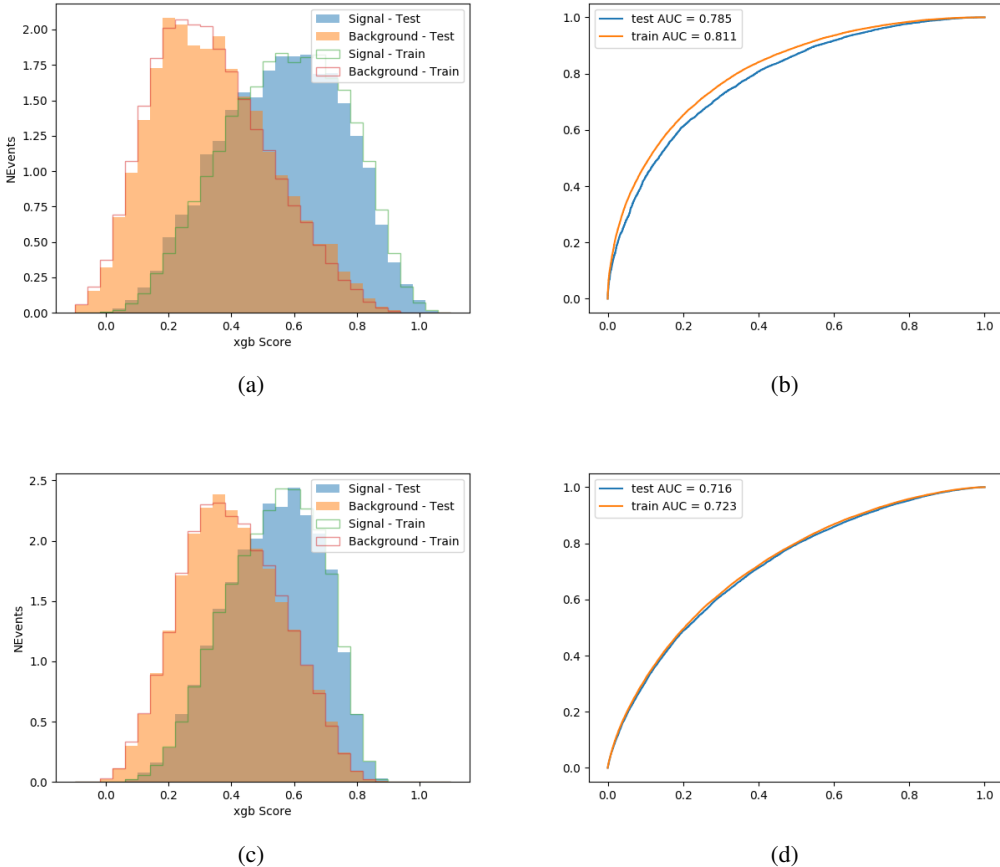


Figure 6.5:

438 **6.3.1 2lSS**439 **6.3.2 3l – Semi – leptonic**440 **6.3.3 3l – Fully – leptonic**441

7 Systematic Uncertainties

442 The systematic uncertainties that are considered are summarized in table ???. These are imple-
 443 mented in the fit either as a normalization factors or as a shape variation or both in the signal
 444 and background estimations. The numerical impact of each of these uncertainties is outlined in
 445 section 8.

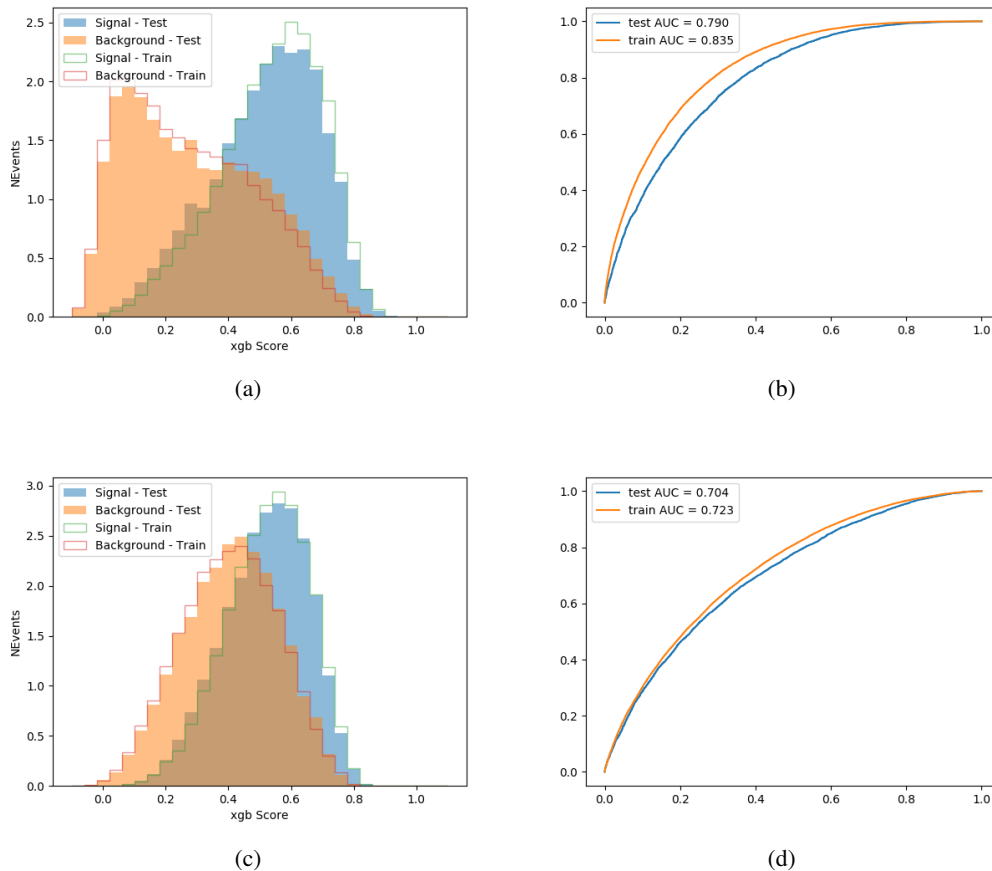


Figure 6.6:

446 The uncertainty in the combined 2015+2016 integrated luminosity is derived from a calibration
 447 of the luminosity scale using x-y beam-separation scans performed in August 2015 and May 2016
 448 [**lumi**].

449 The experimental uncertainties are related to the reconstruction and identification of light leptons
 450 and b-tagging of jets, and to the reconstruction of E_T^{miss} . The sources which contribute to the
 451 uncertainty in the jet energy scale [**jes**] are decomposed into uncorrelated components and treated
 452 as independent sources in the analysis.

453 The uncertainties in the b-tagging efficiencies measured in dedicated calibration analyses
 454 [**btag_cal**] are also decomposed into uncorrelated components. The large number of components
 455 for b-tagging is due to the calibration of the distribution of the BDT discriminant.

456 The systematic uncertainties associated with the signal and background processes are accounted
 457 for by varying the cross-section of each process within its uncertainty.

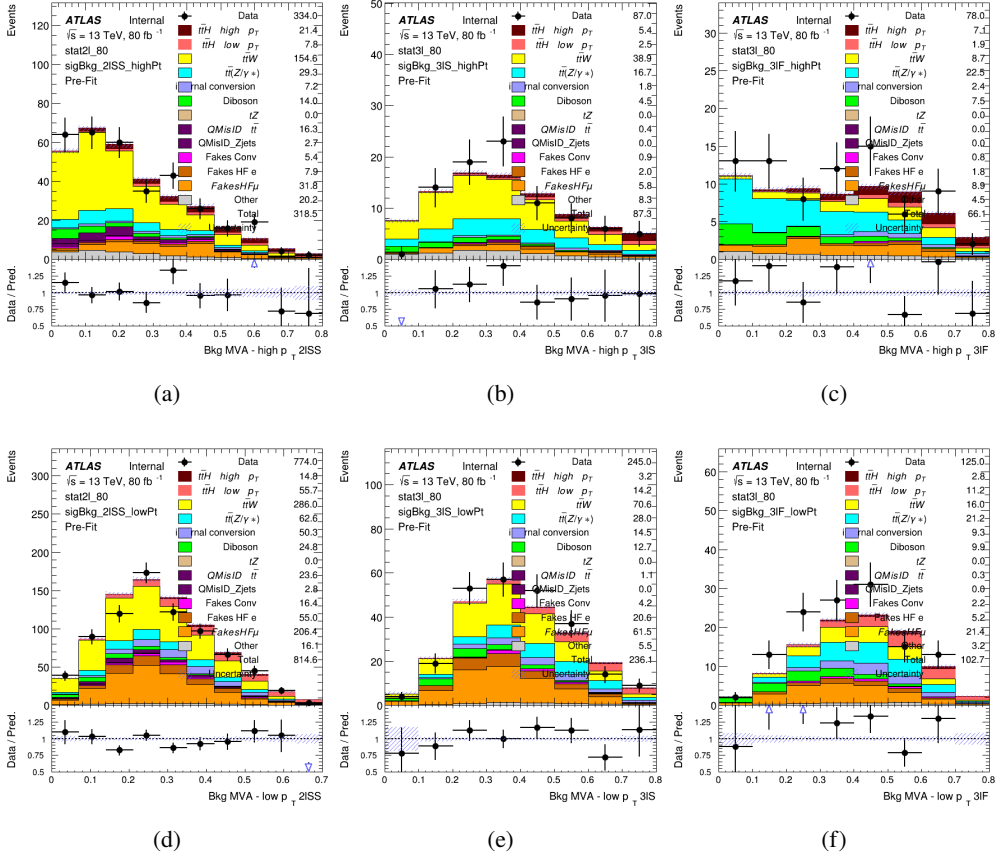


Figure 6.7: scores

458 8 Results

459 Unblinded results are shown for the 80 fb^{-1} data set, as well as MC only projections of results
 460 using the full Run-2, 140 fb^{-1} dataset.

461 8.1 Results - 80 fb^{-1}

462 A maximum likelihood fit is performed simultaneously over the regions shown in figure 8.1.

Table 16: Sources of systematic uncertainty considered in the analysis. Some of the systematic uncertainties are split into several components, as indicated by the number in the rightmost column.

Systematic uncertainty	Components
Luminosity	1
Pileup reweighting	1
Physics Objects	
Electron	6
Muon	15
Jet energy scale and resolution	28
Jet vertex fraction	1
Jet flavor tagging	131
E_T^{miss}	3
Total (Experimental)	186
Background Modeling	
Cross section	24
Renormalization and factorization scales	10
Parton shower and hadronization model	2
Shower tune	4
Total (Signal and background modeling)	40
Background Modeling	
Cross section	24
Renormalization and factorization scales	10
Parton shower and hadronization model	2
Shower tune	4
Total (Signal and background modeling)	40
Total (Overall)	226

463 8.2 Projected Results - 140 fb^{-1}

464 9 Conclusion

465 As search for the effects of dimension-six operators on $t\bar{t}H$ production is performed. An effective
 466 field theory approached is used to parameterize the effects of high energy physics on the Higgs
 467 momentum spectrum. The momentum spectrum is reconstructed using various MVA techniques,
 468 and the limits on dimension-six operators are limited to X.

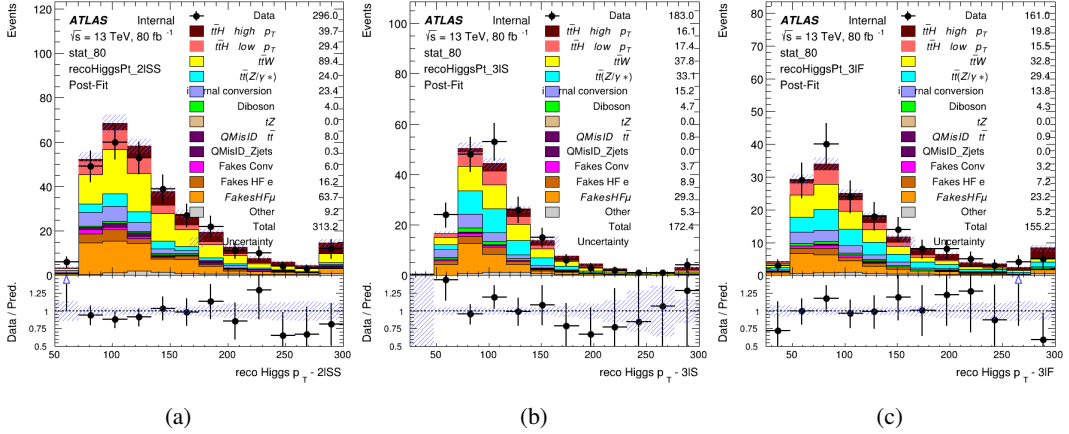


Figure 8.1:

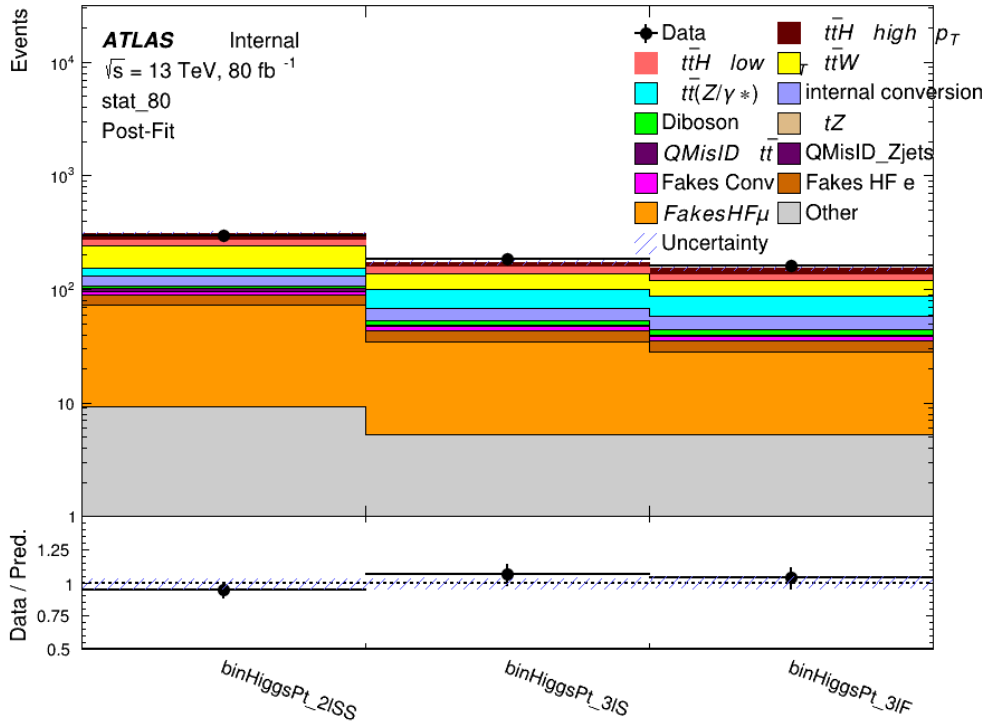


Figure 8.2: Post-fit summary of fit.

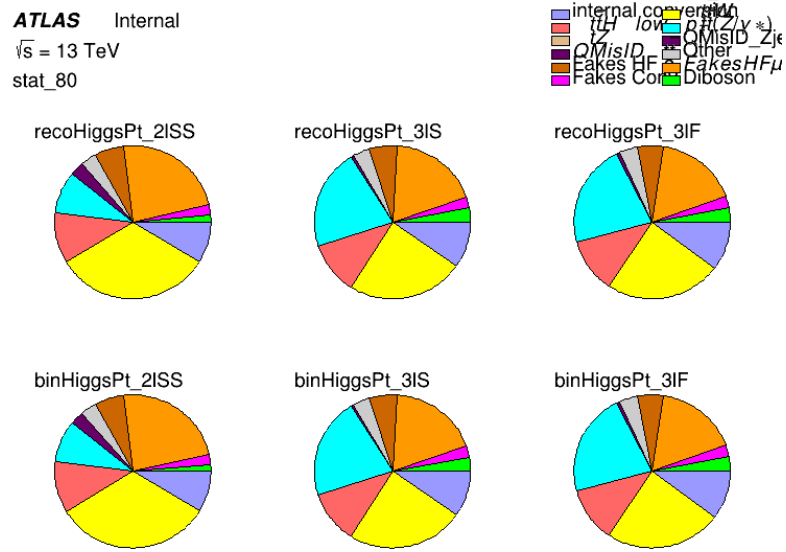


Figure 8.3: Background composition of the fit regions.

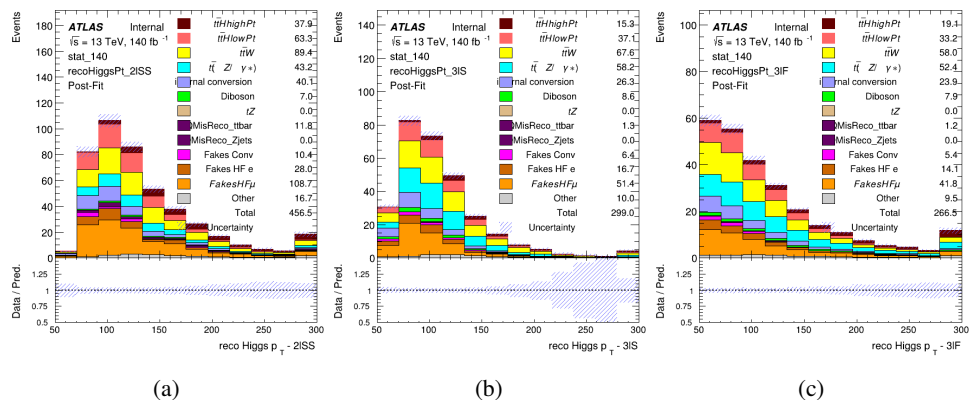


Figure 8.4:

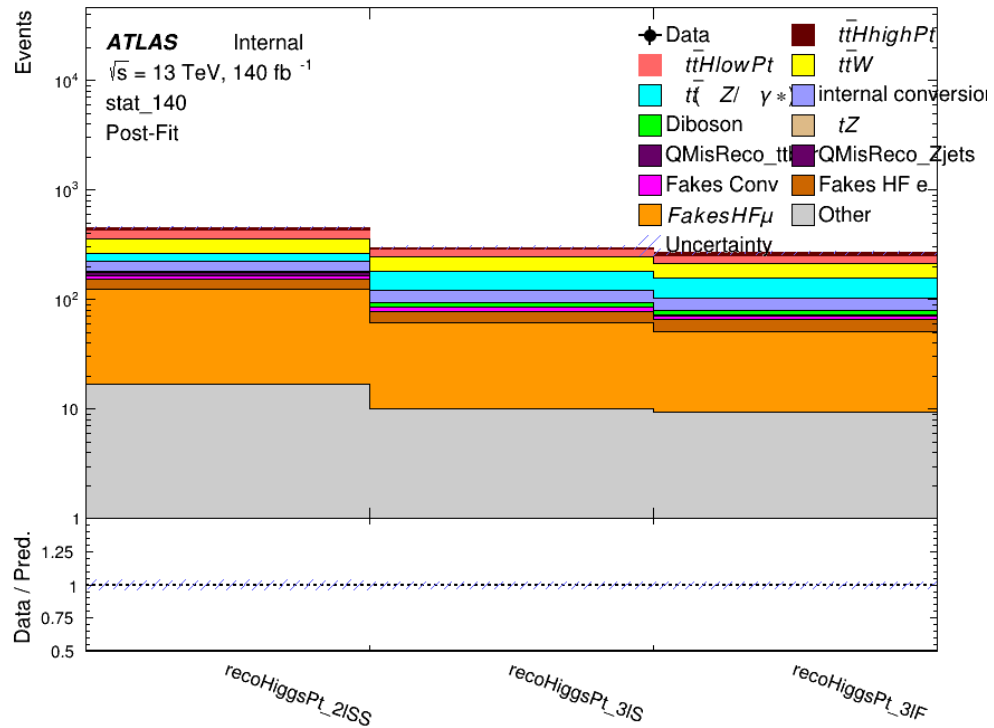


Figure 8.5: Post-fit summary of fit.

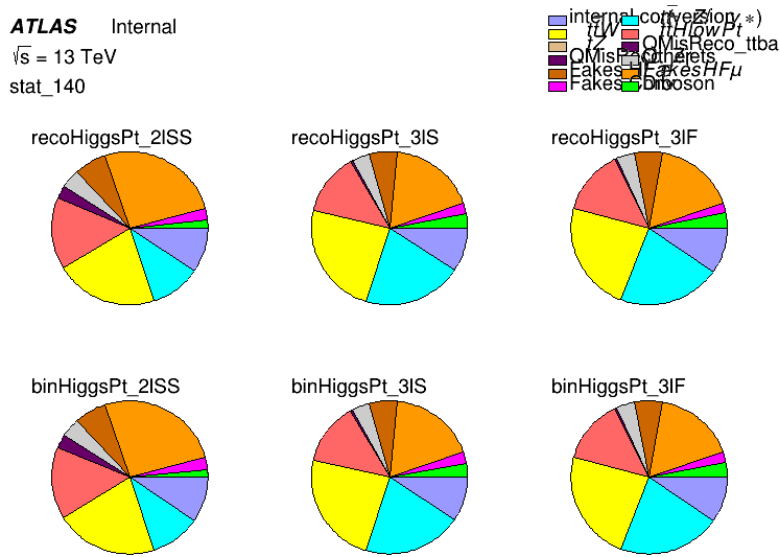


Figure 8.6: Background composition of the fit regions.

469 List of contributions

470

⁴⁷¹ **Appendices**

⁴⁷² **A Machine Learning Models**

⁴⁷³ The following section provides details of the various MVAs as well as a few studies performed in
⁴⁷⁴ support of this analysis, exploring alternate decisions and strategies.

⁴⁷⁵ **A.1 Higgs Reconstruction Models**

⁴⁷⁶ **A.1.1 b-jet Identification Features - 2lSS**

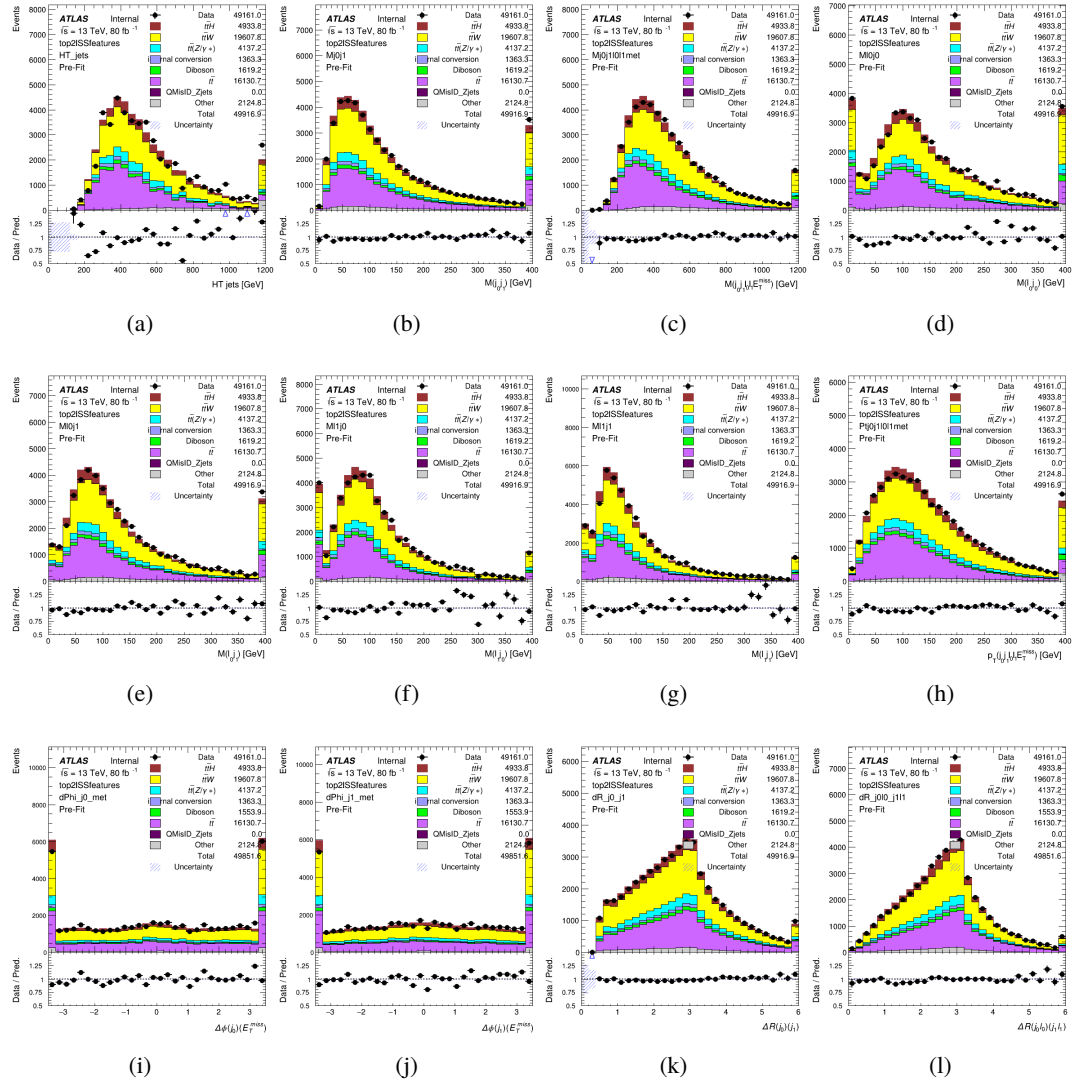


Figure A.1: Input features for top2lSS

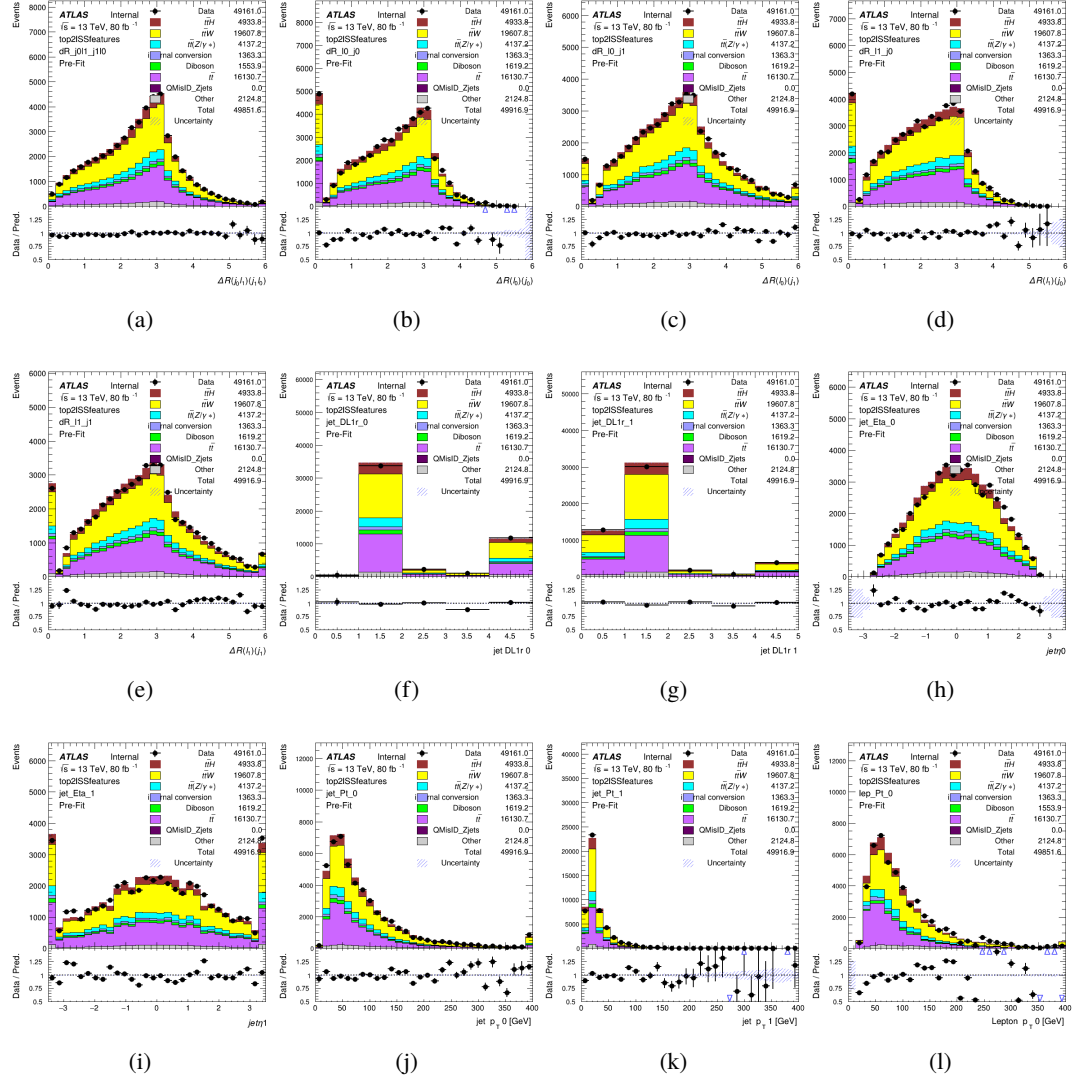


Figure A.2: Input features for top2lSS

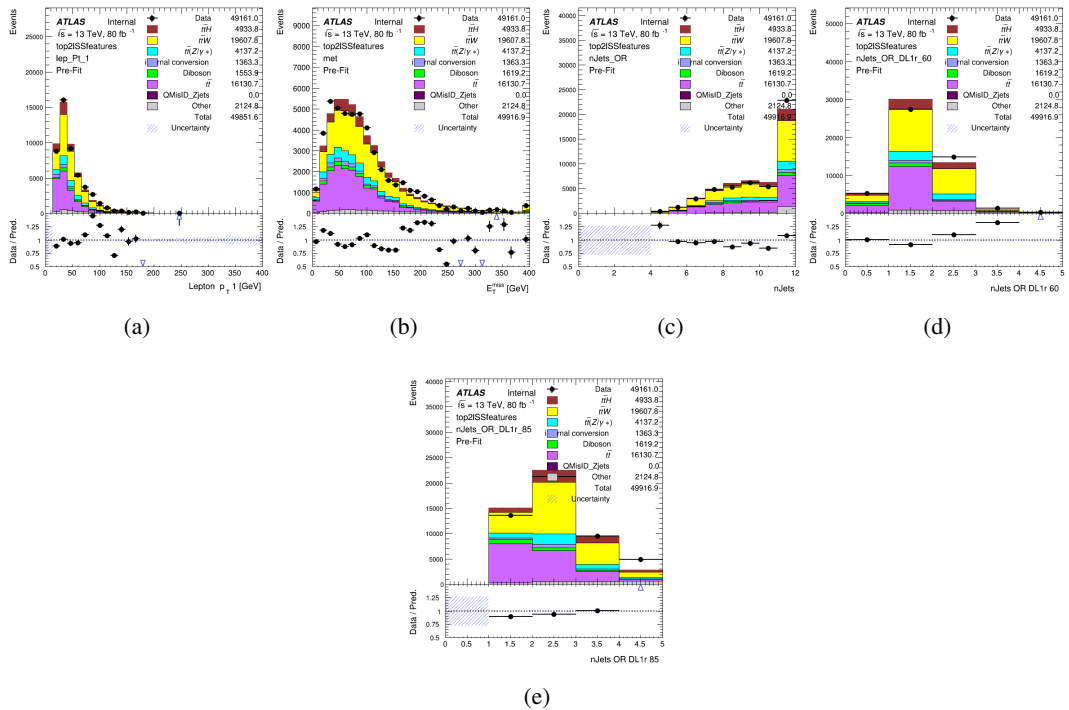


Figure A.3: Input features for top2lSS

⁴⁷⁷ **A.1.2 b-jet Identification Features - 3l**

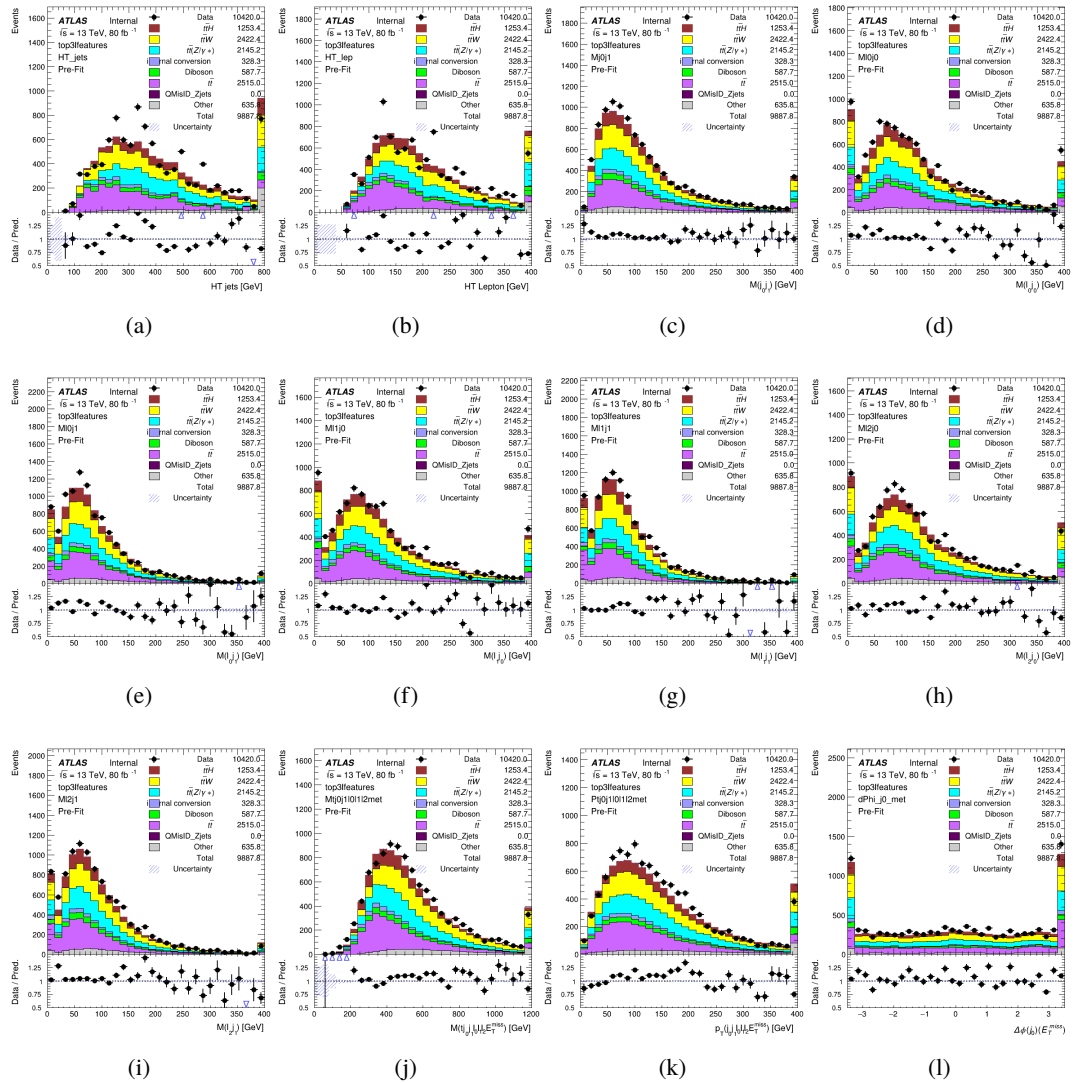


Figure A.4: Input features for top31

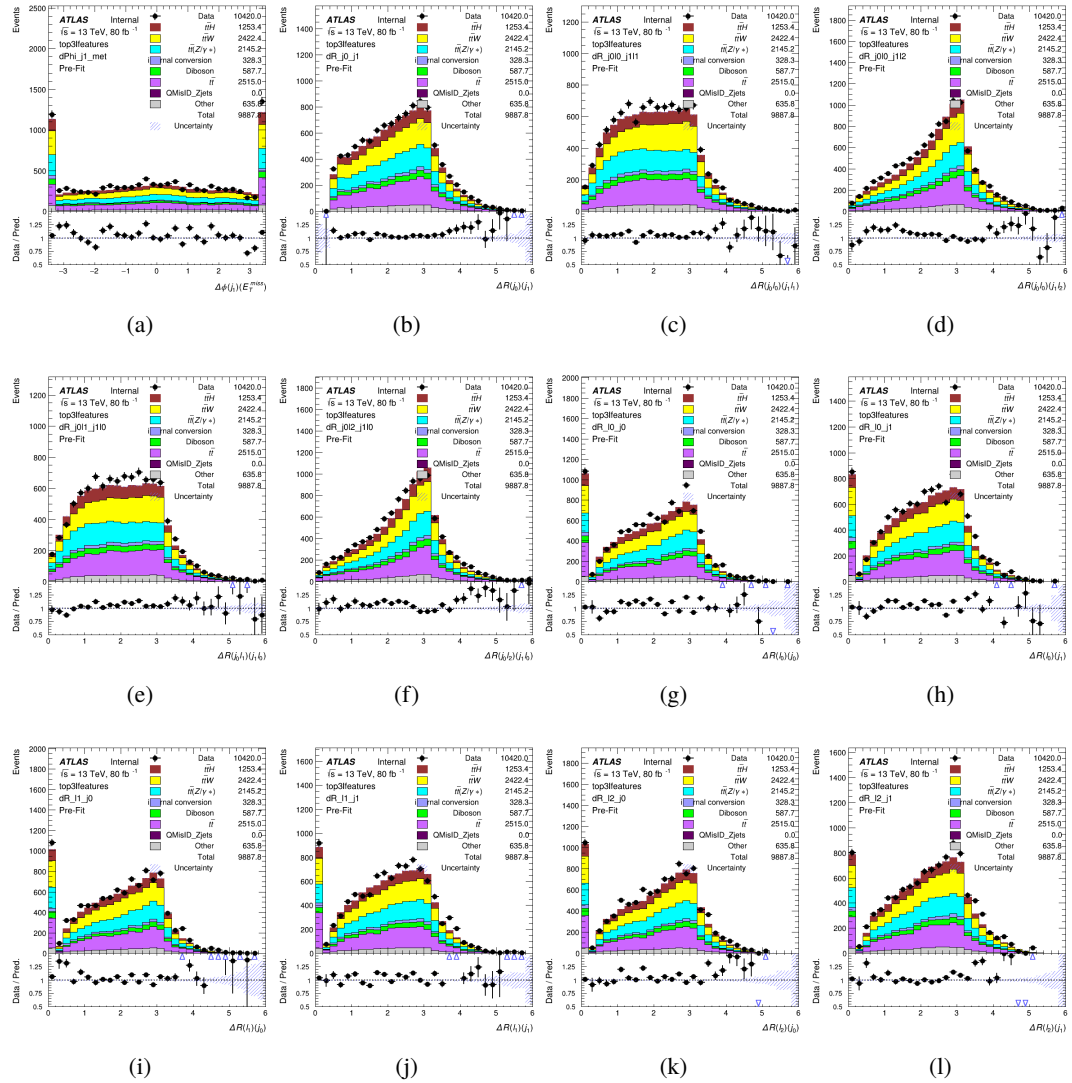


Figure A.5: Input features for top31

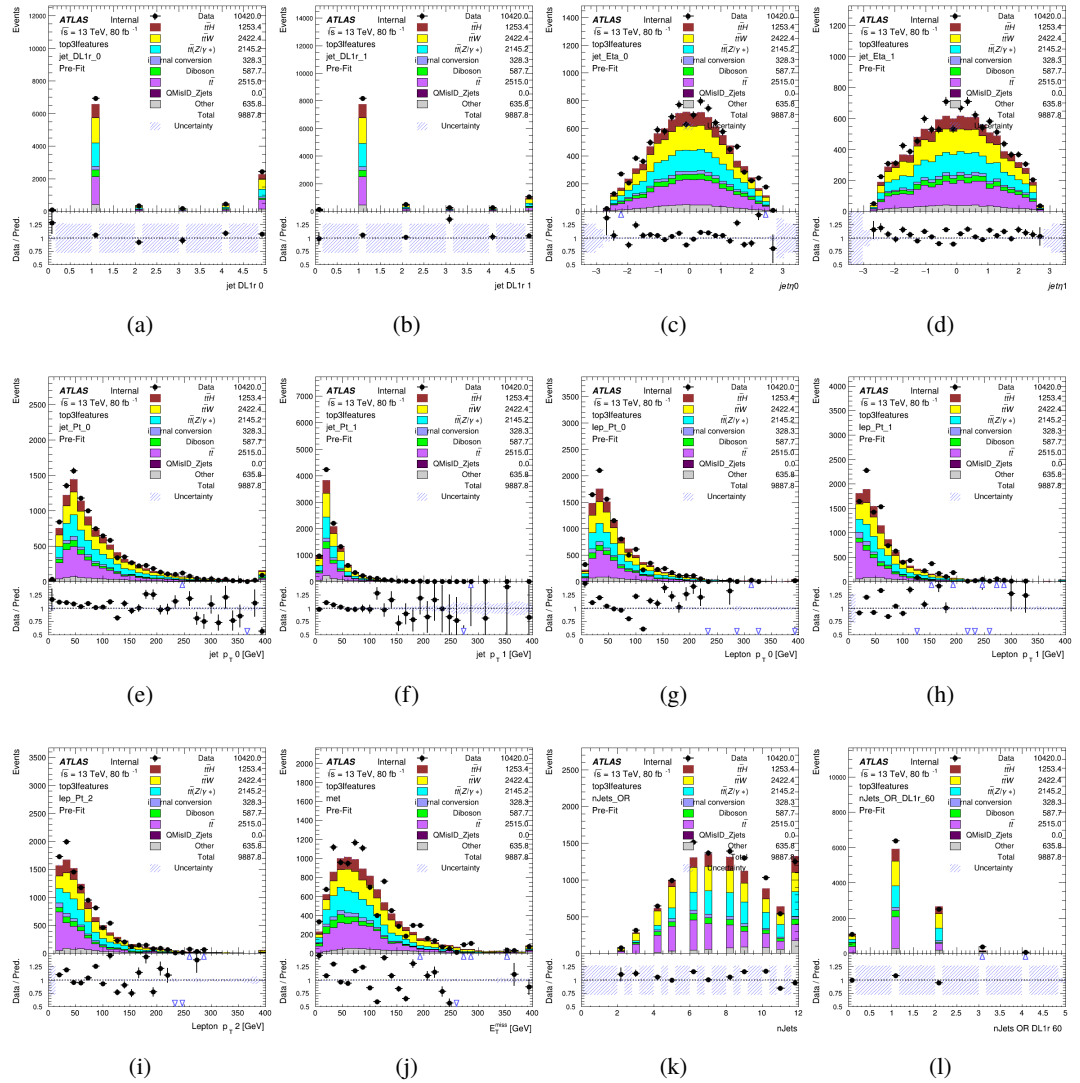
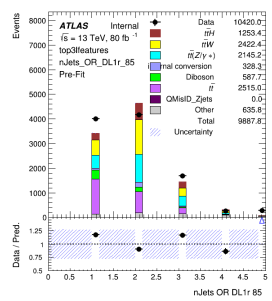


Figure A.6: Input features for top31



(a)

Figure A.7: Input features for top3l

⁴⁷⁸ **A.1.3 Higgs Reconstruction Features - 2lSS**

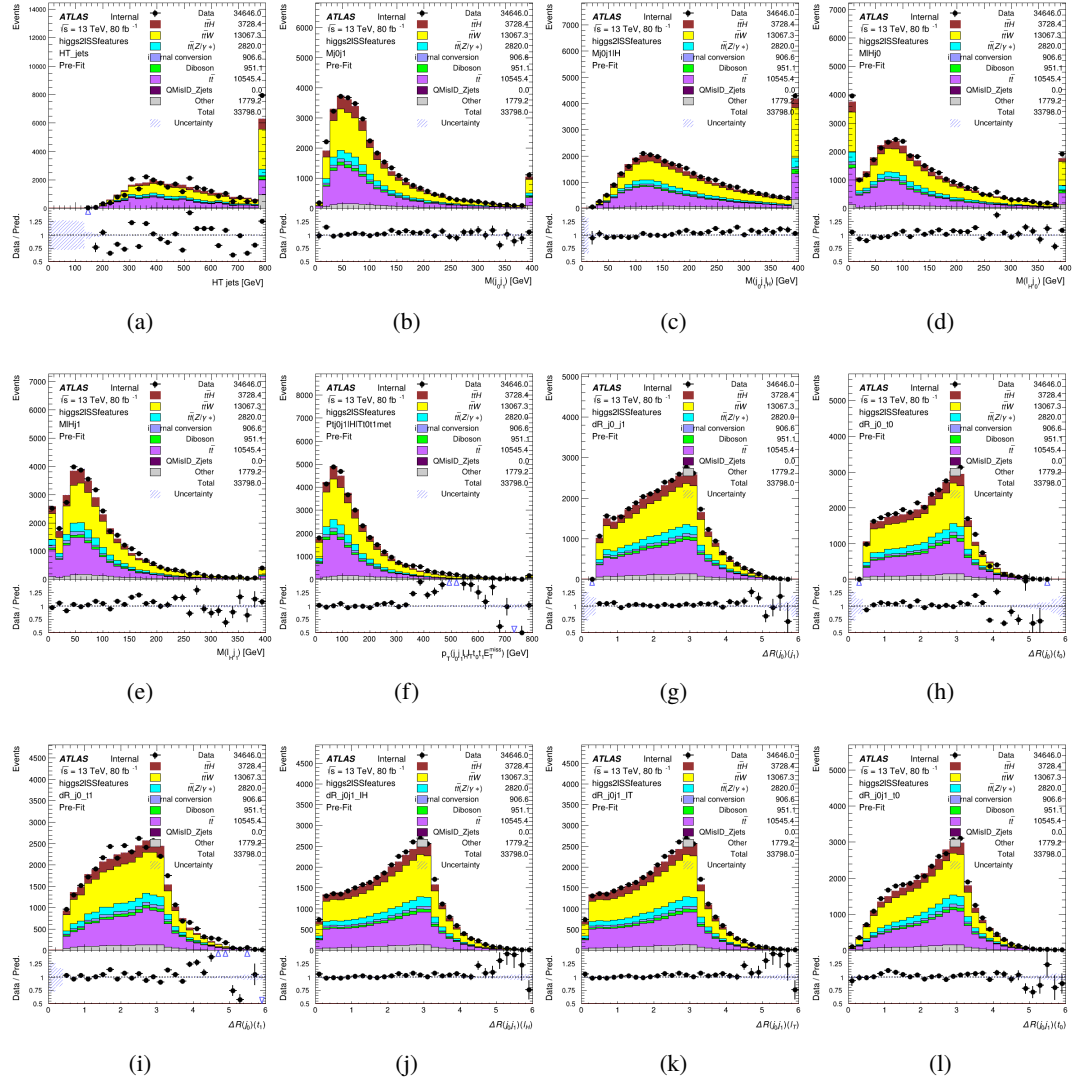


Figure A.8: Input features for higgs2lSS

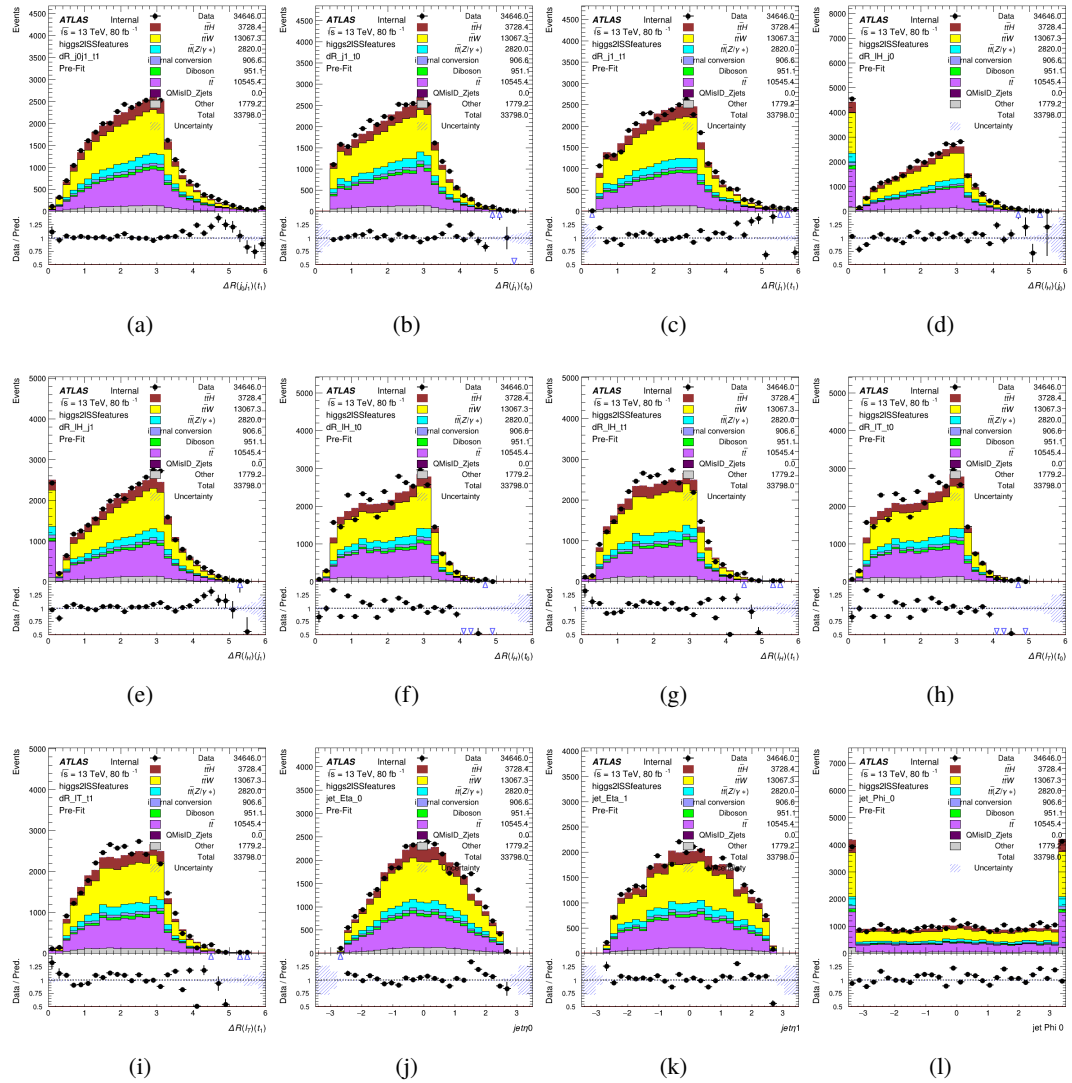


Figure A.9: Input features for higgs2lSS

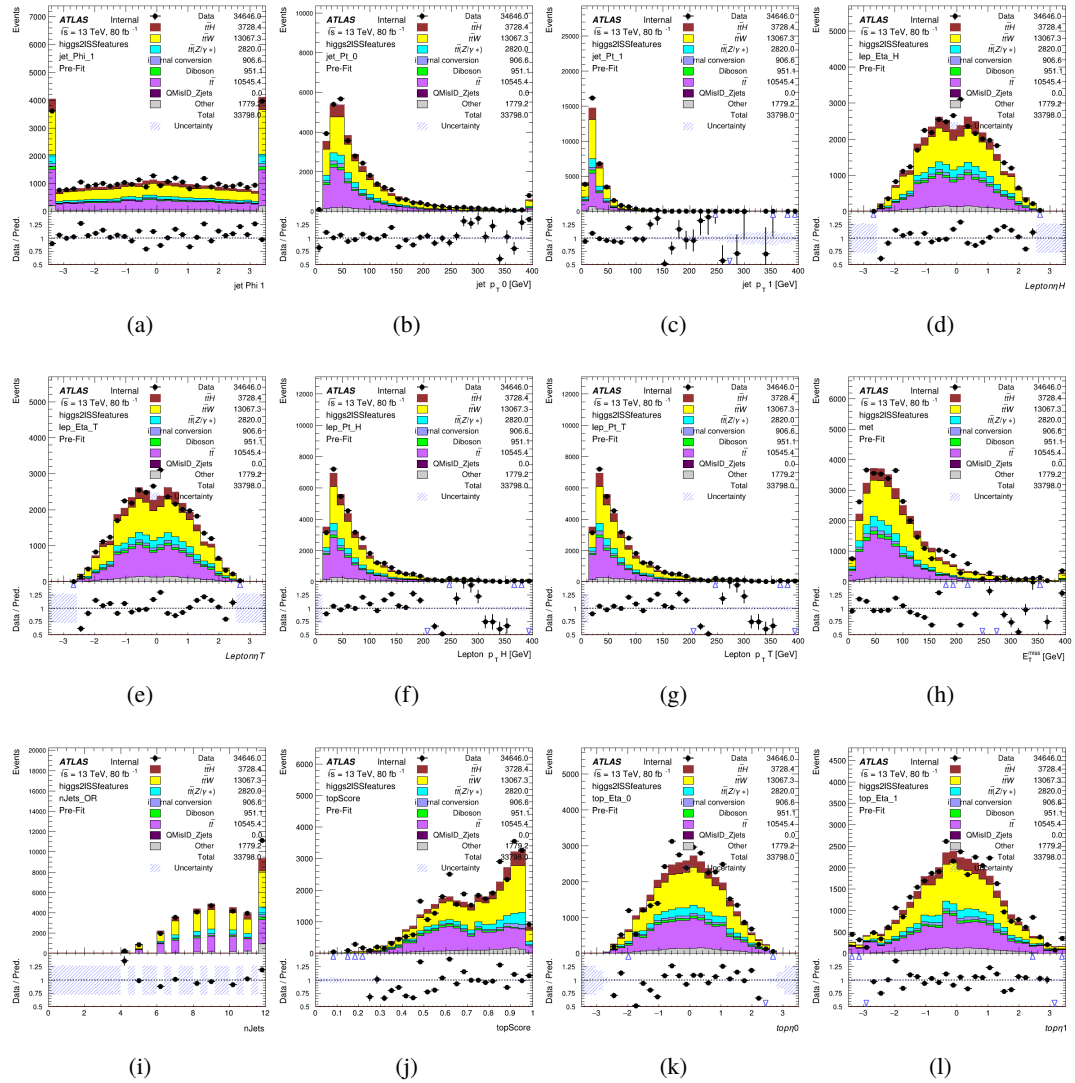


Figure A.10: Input features for higgs2ISS

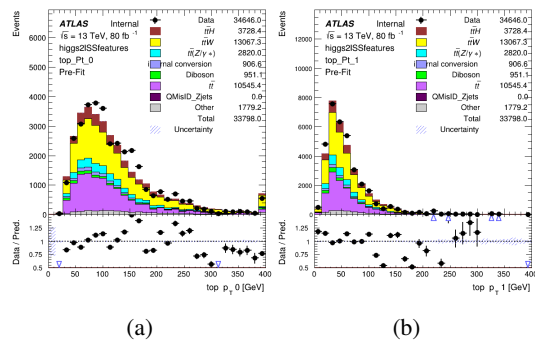


Figure A.11: Input features for higgs2ISS

⁴⁷⁹ **A.1.4 Higgs Reconstruction Features - 3lS**

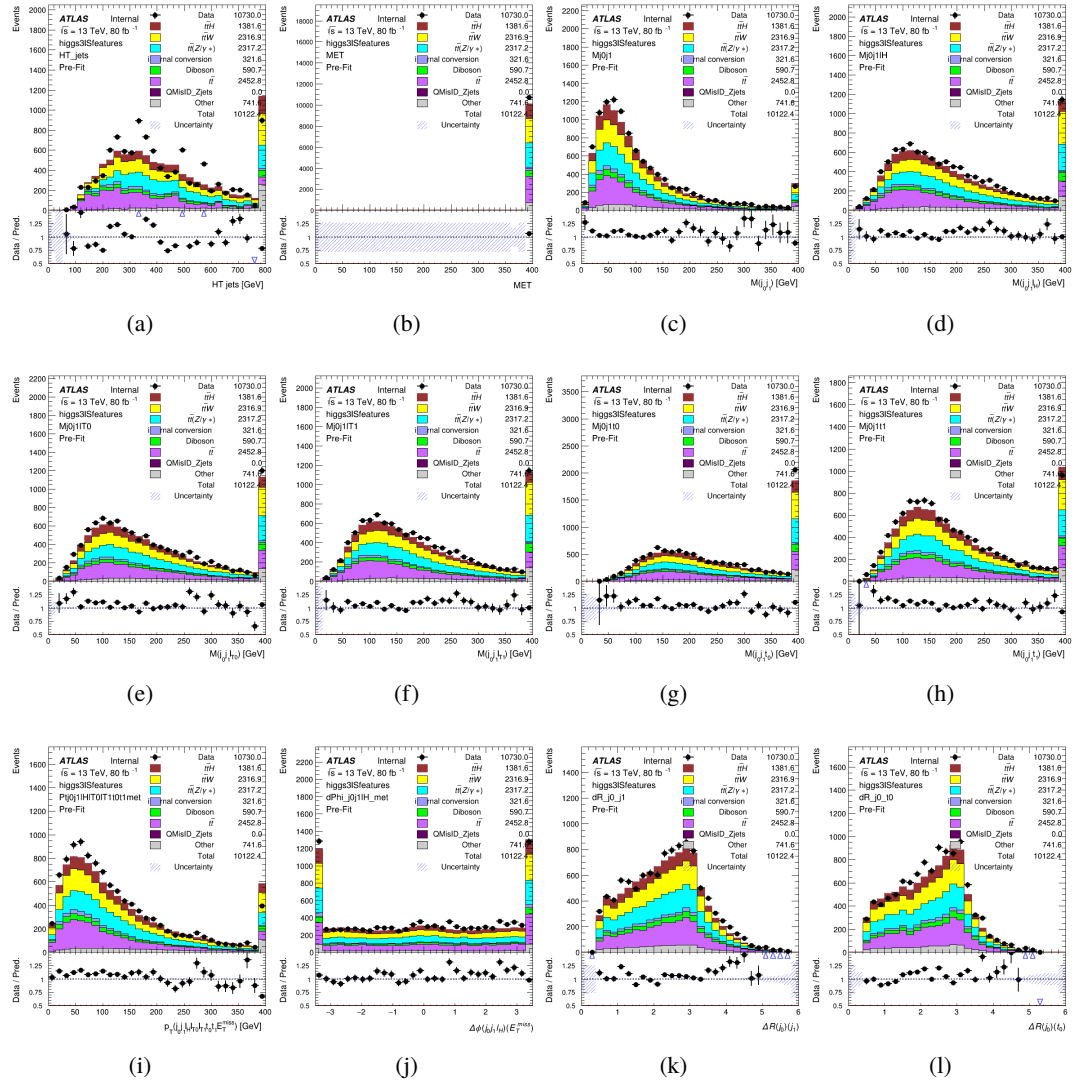


Figure A.12: Input features for higgs3IS

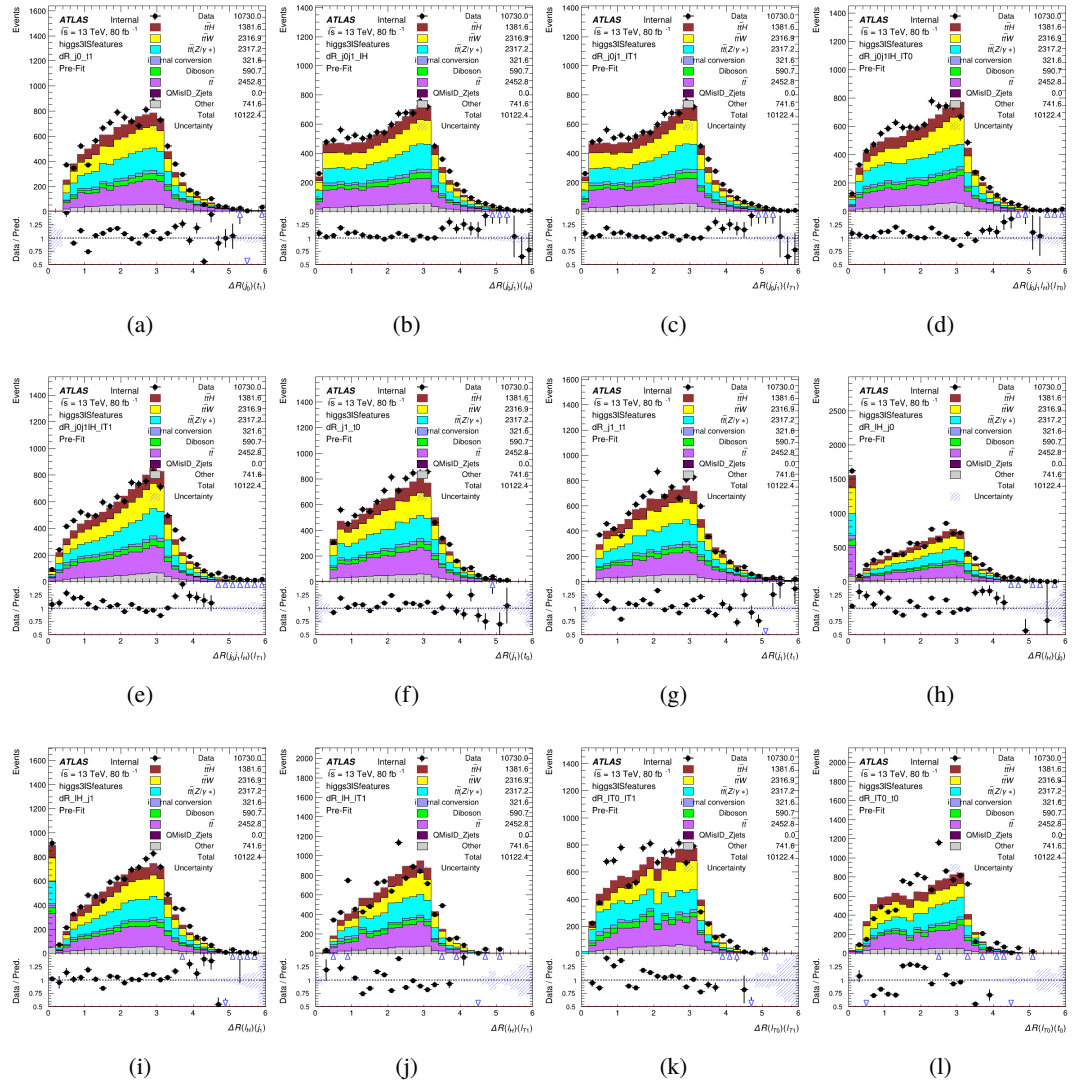


Figure A.13: Input features for higgs3lS

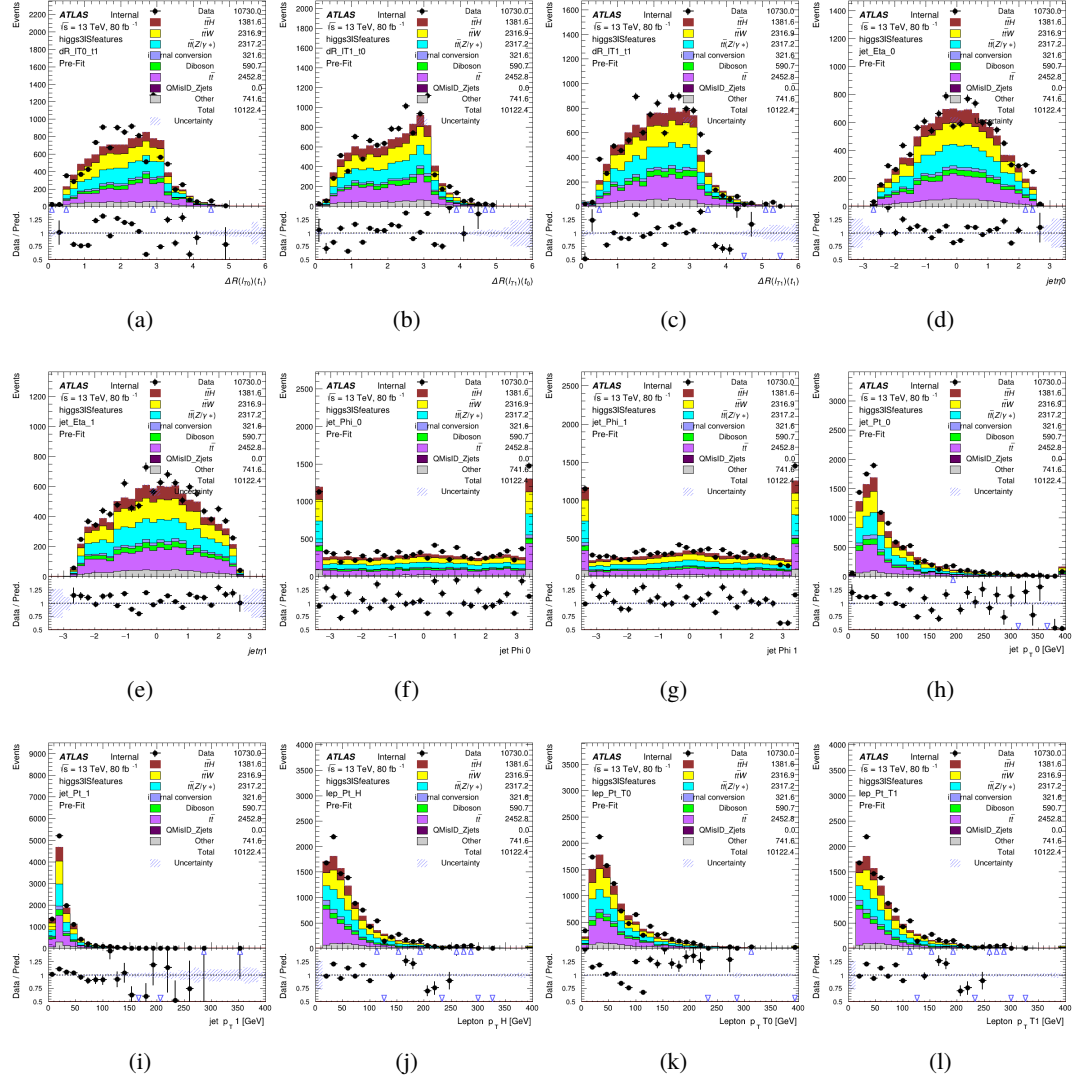


Figure A.14: Input features for higgs3lS

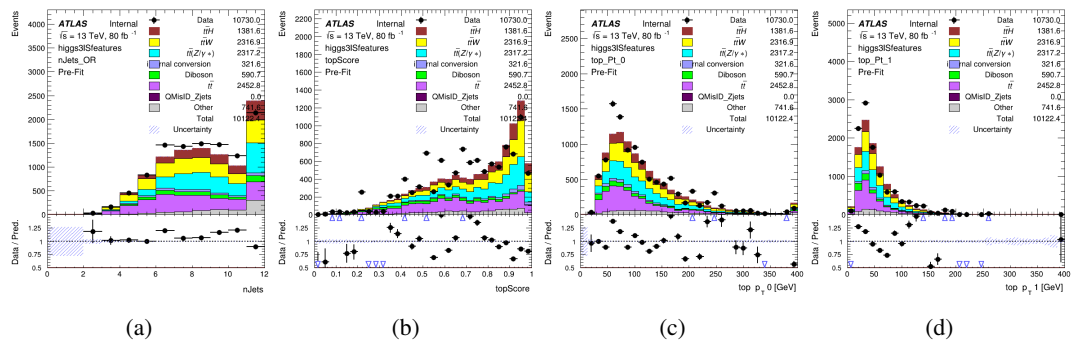


Figure A.15: Input features for higgs31S

480 **A.1.5 Higgs Reconstruction Features - 3lF**

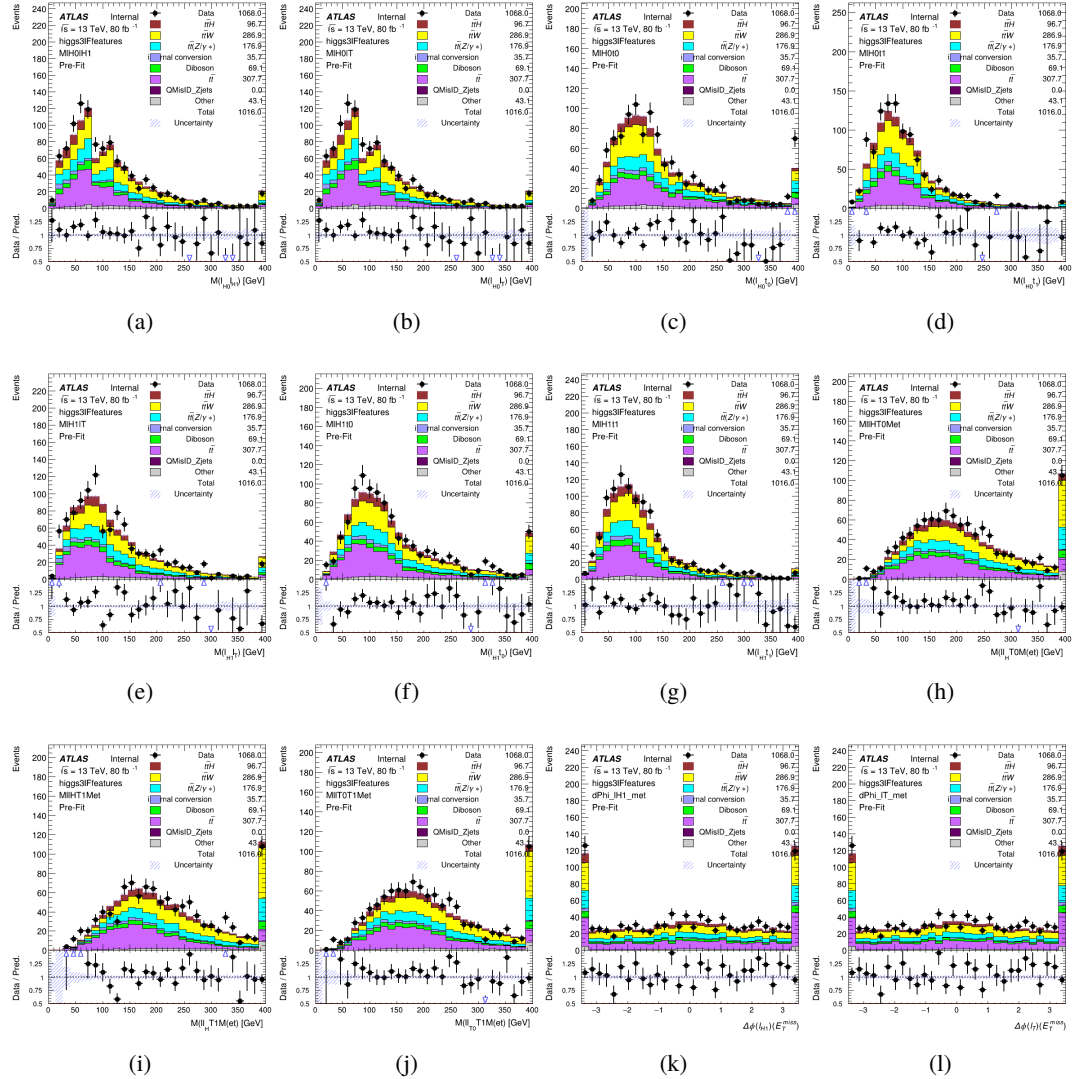


Figure A.16: Input features for higgs3IF

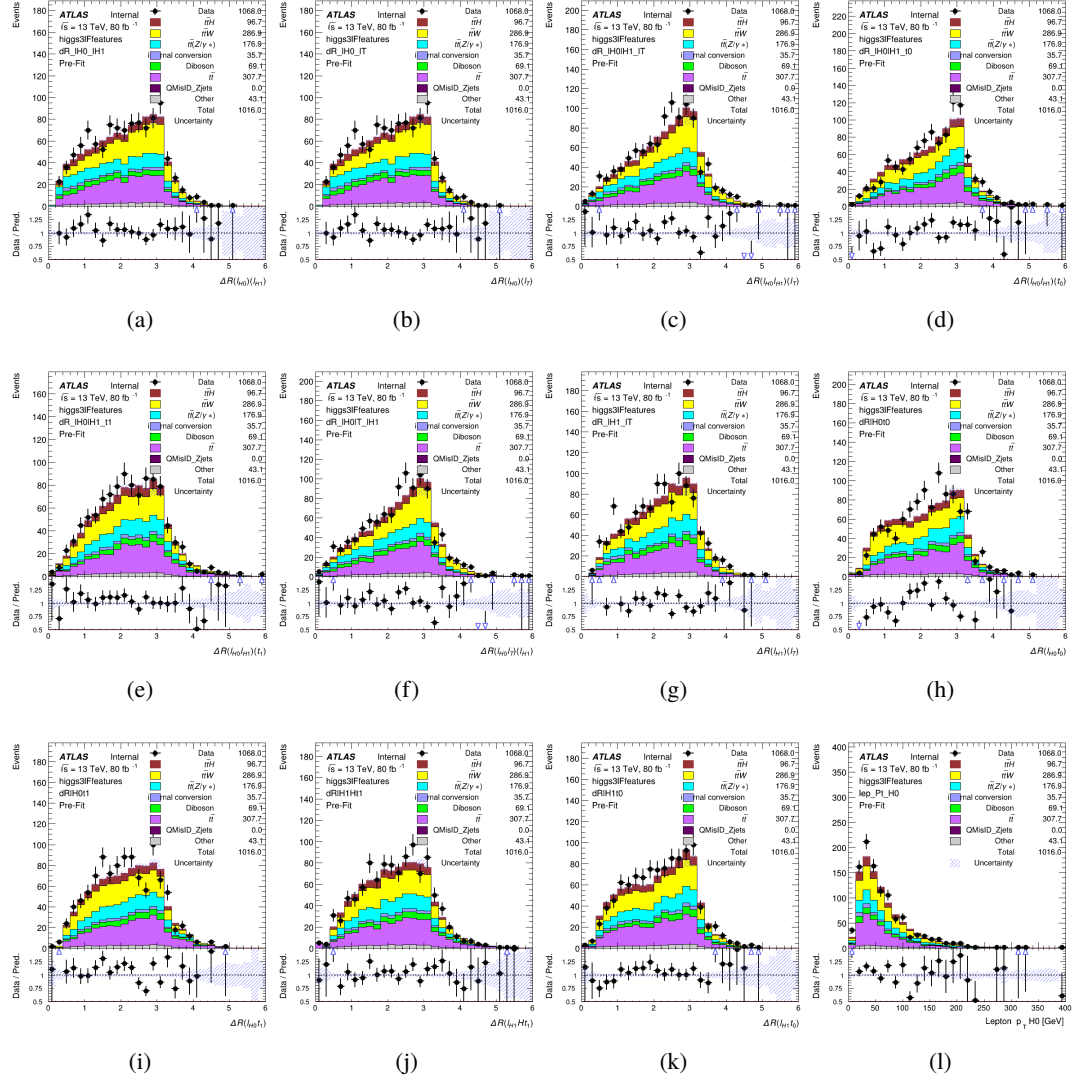


Figure A.17: Input features for higgs3lF

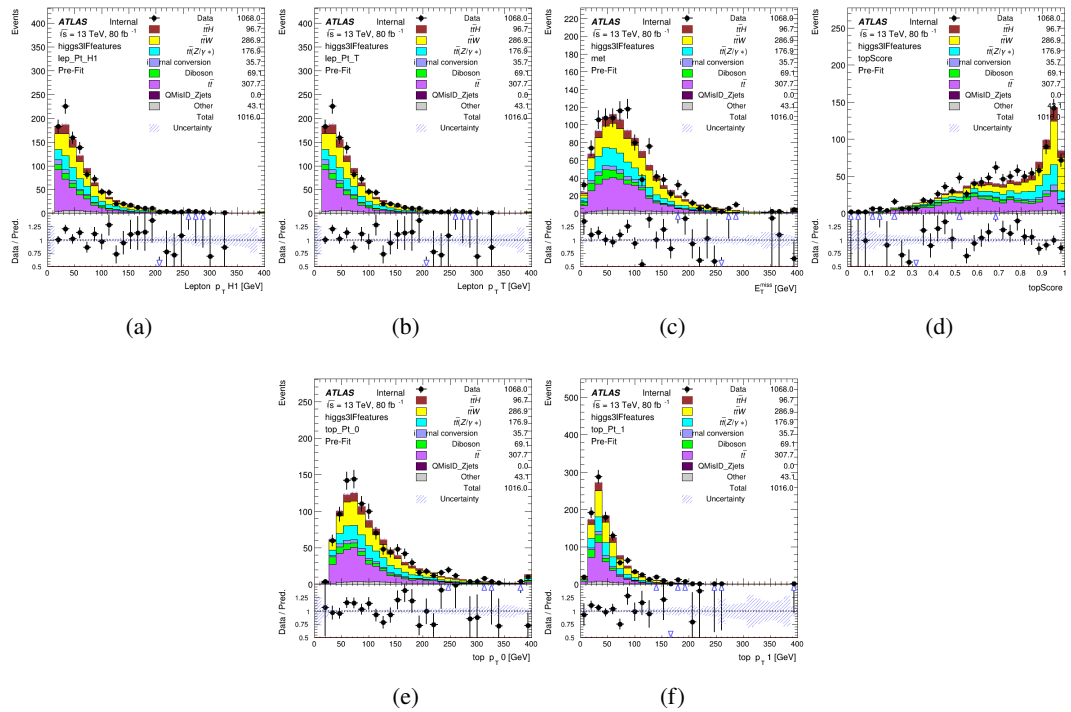


Figure A.18: Input features for higgs3IF

481 **A.2 Background Rejection MVAs**

482 **A.2.1 Background Rejection MVA Features - 2lSS**

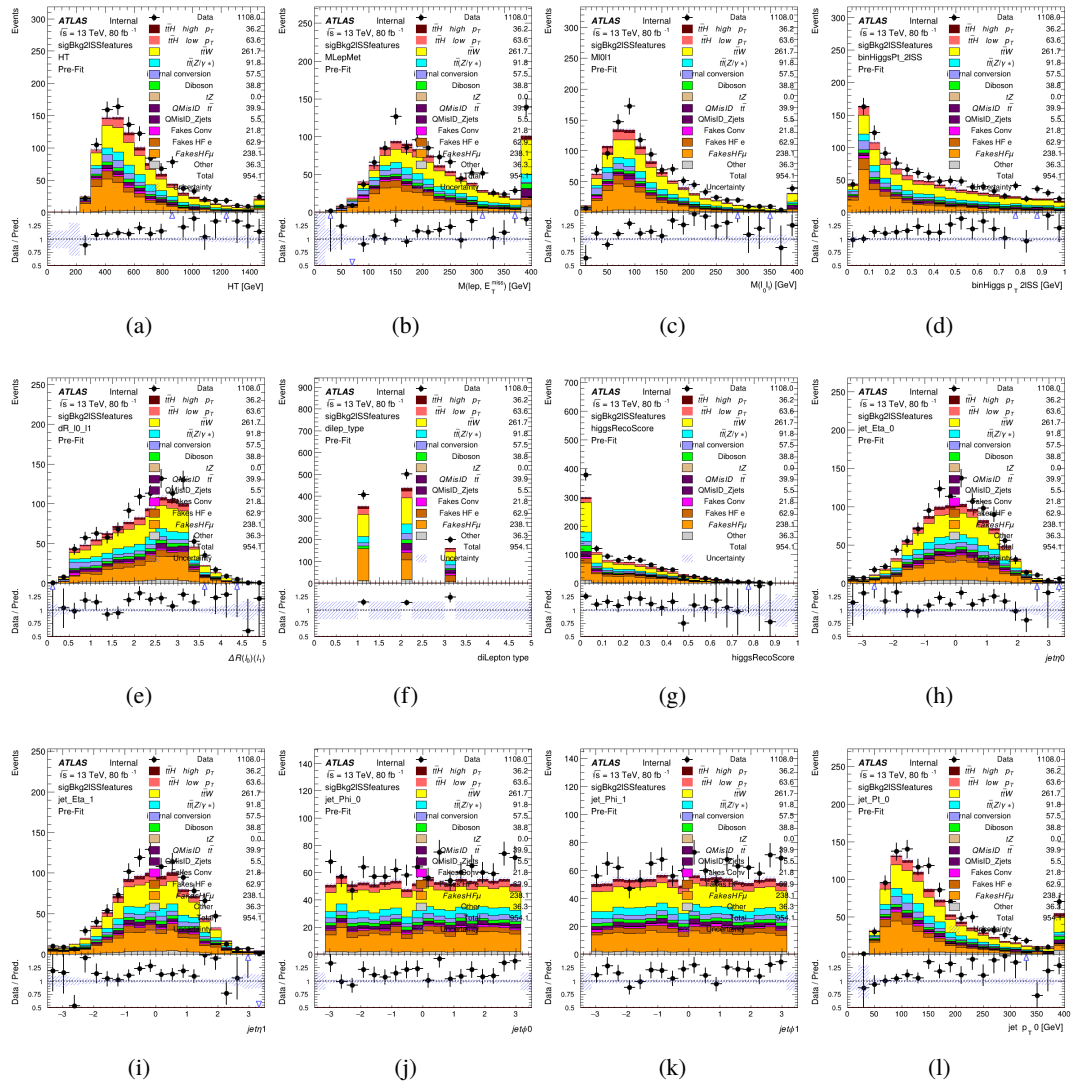


Figure A.19: Input features for sigBkg2lSS

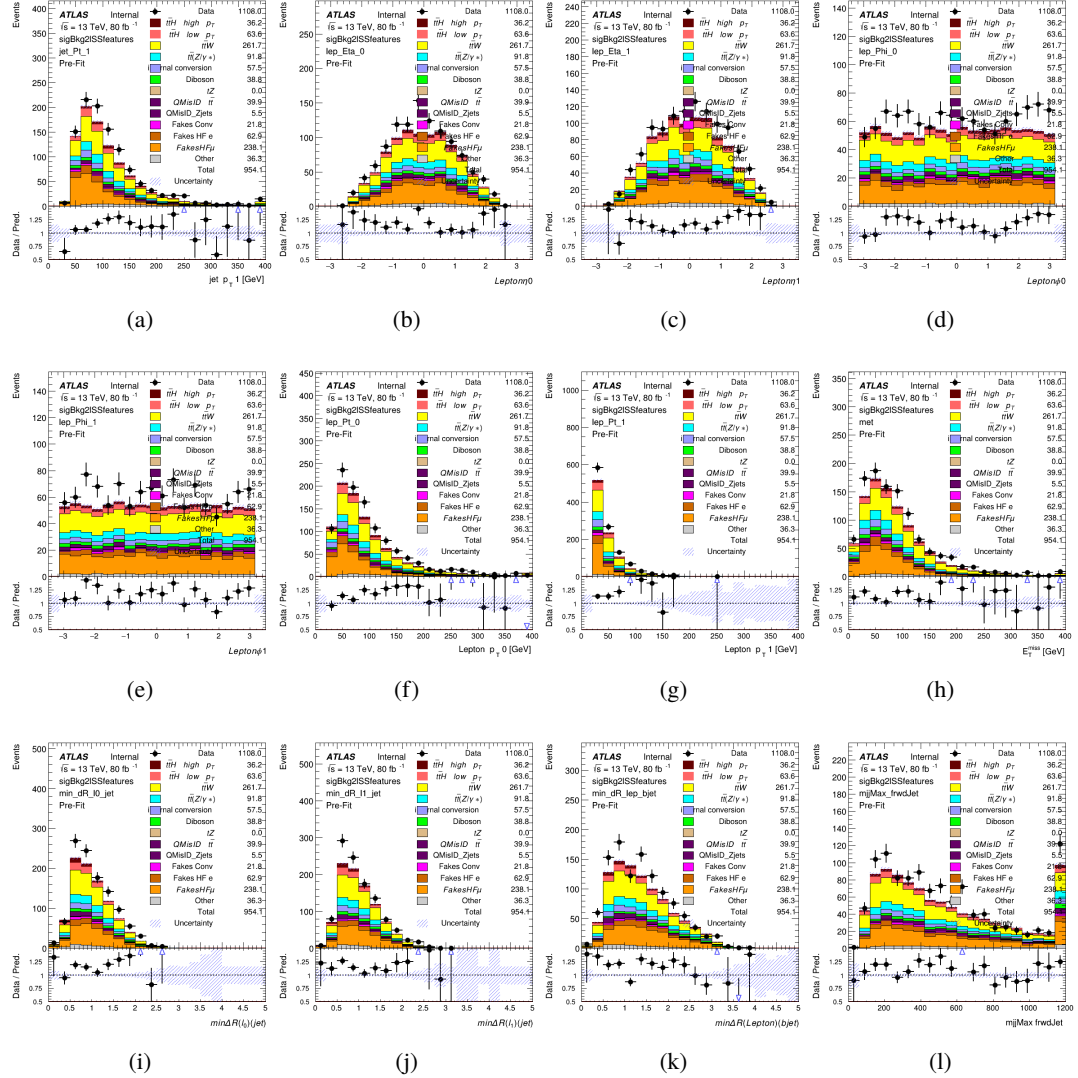


Figure A.20: Input features for sigBkg2lSS

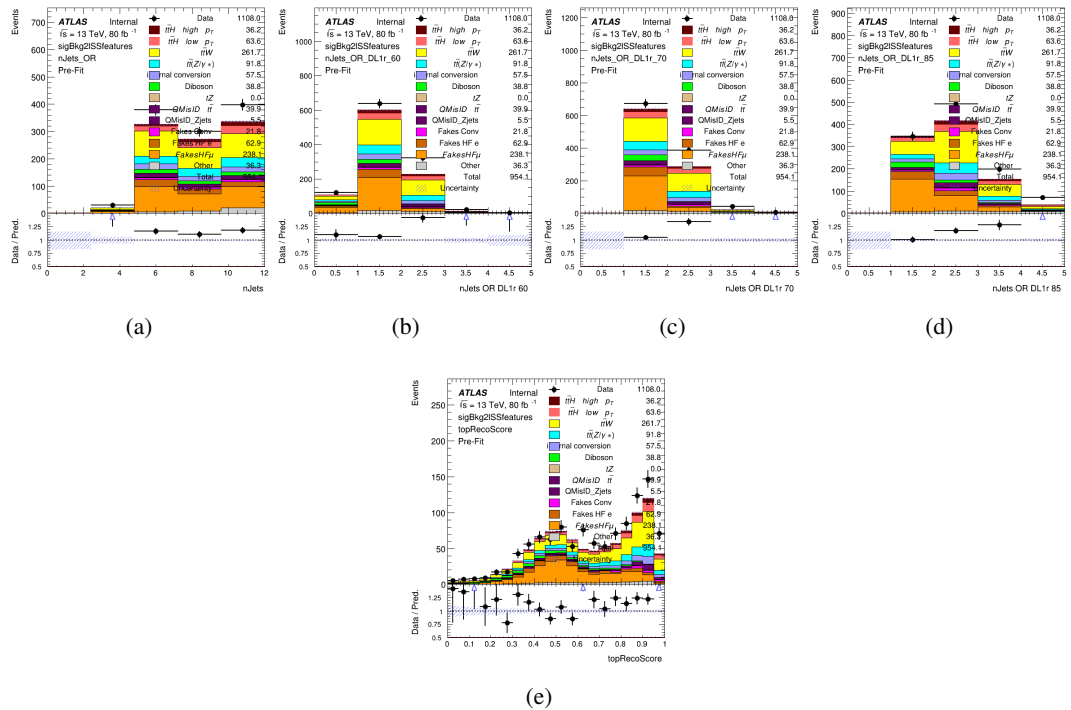


Figure A.21: Input features for sigBkg2ISS

483 **A.2.2 Background Rejection MVA Features - 3l**

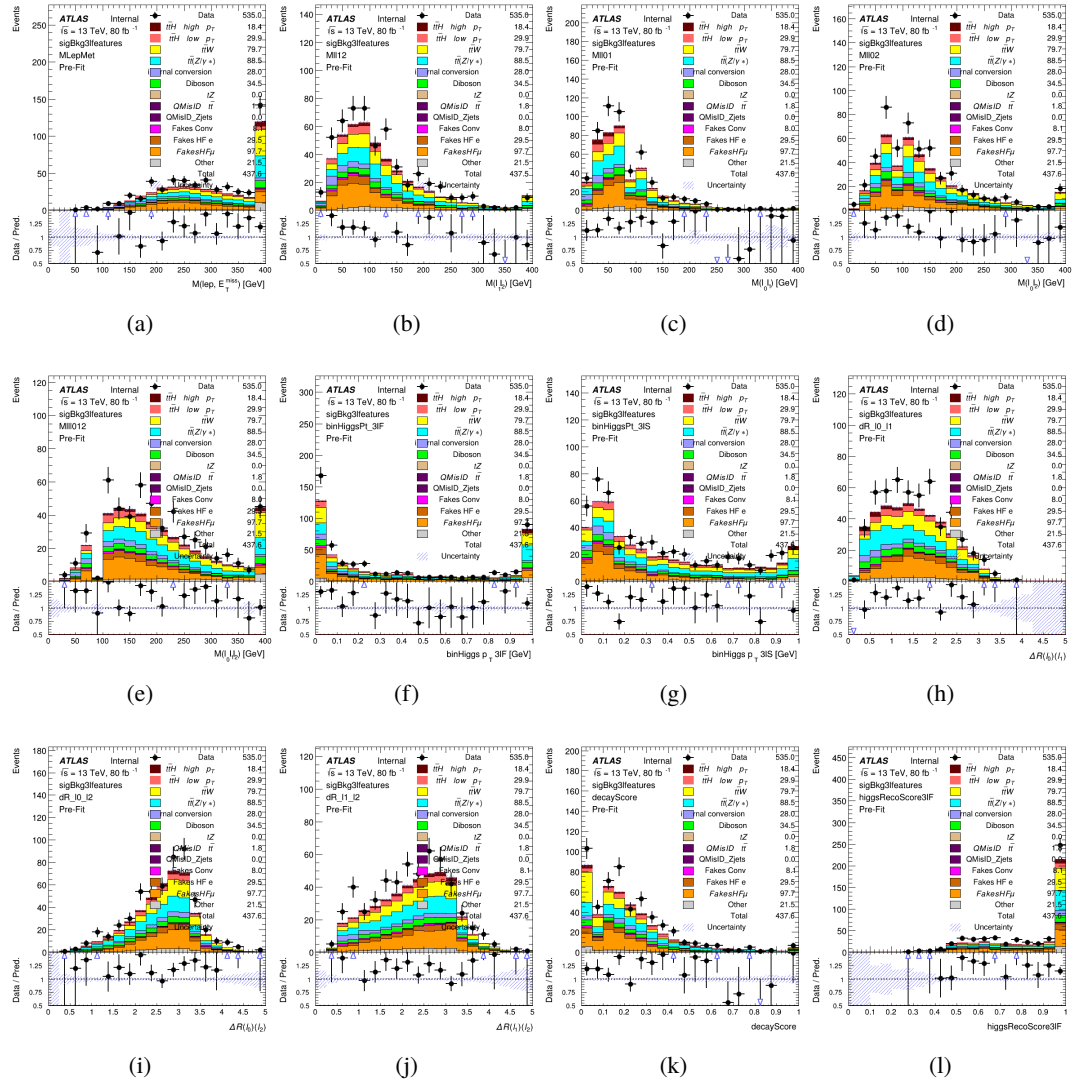


Figure A.22: Input features for sigBkg3l

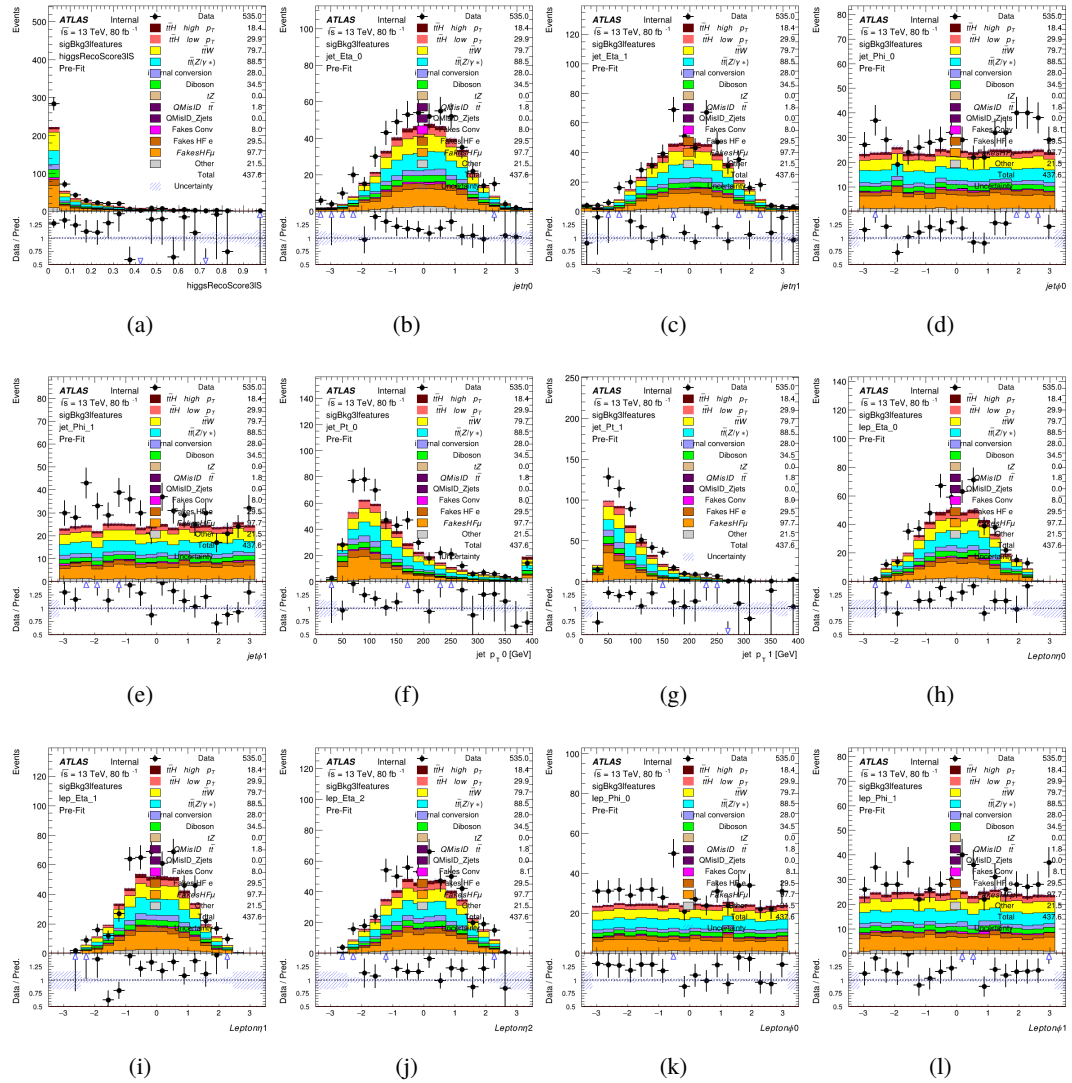


Figure A.23: Input features for sigBkg3l

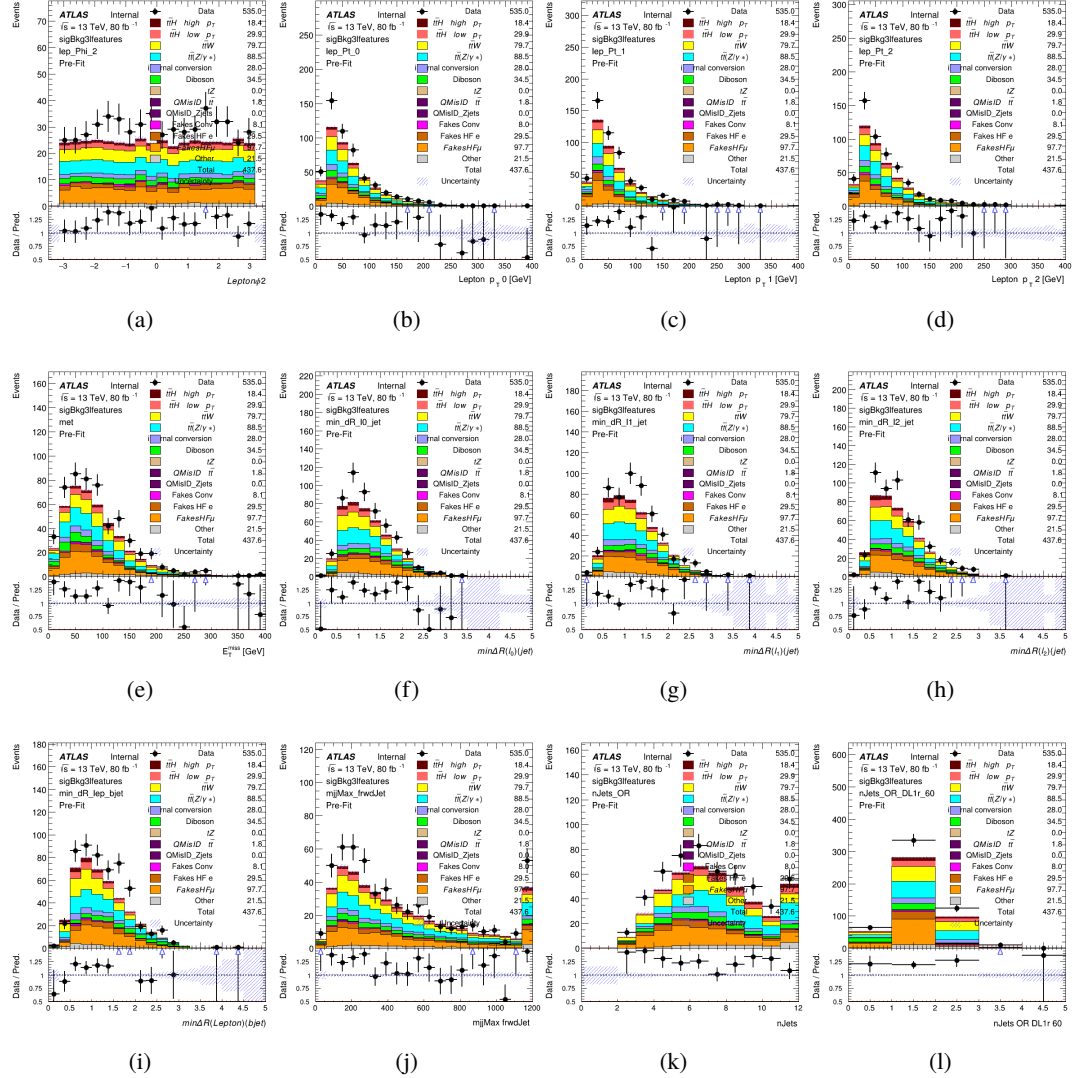


Figure A.24: Input features for sigBkg3l

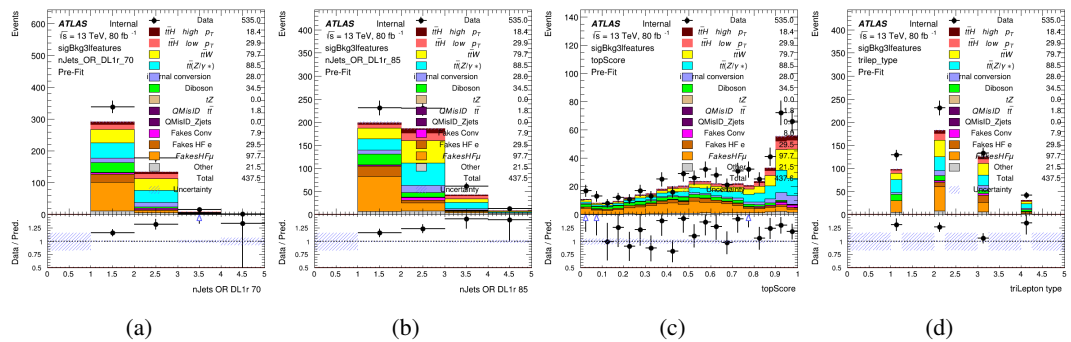


Figure A.25: Input features for sigBkg3l

484 **A.3 Alternate b-jet Identification Algorithm**

485 The nominal analysis reconstructs the b-jets by considering different combinations of jets, and
486 asking a neural network to determine whether each combination consists of b-jets from top quark
487 decays. An alternate approach would be to give the neural network about all of the jets in an event
488 at once, and train it to select which two are most likely to be the b-jets from top decay. It was
489 hypothesized that this could perform better than considering each combination independently, as
490 the neural network could consider the event as a whole. While this is not found to be the case,
491 these studies are documented here as a point of interest and comparison.

492 For these studies, the kinematics of the 10 highest p_T jets in each event are used for training. This
493 includes the vast majority of truth b-jets. Specifically the p_T , η , ϕ , E , and DL1r score of each jet
494 are used. For events with fewer than 10 jets, these values are substituted with 0. The p_T , η , ϕ ,
495 and E of the leptons and E_T^{miss} are included as well. Categorical cross entropy is used as the loss
496 function.

Table 17: Accuracy of the NN in identifying b-jets from tops in 2lSS events for the alternate categorical method compared to the nominal method.

Channel	Categorical	Nominal
2lSS	70.6%	73.9%
3l	76.1%	79.8%

497 **A.4 Binary Classification of the Higgs p_T**

498 A two bin fit of the Higgs momentum is used because statistics are insufficient for any finer
499 resolution. This means separating high and low p_T events is sufficient for this analysis. As such,
500 rather than attempting the reconstruct the full Higgs p_T spectrum, a binary classification approach
501 is explored.

502 A model is built to determine whether $t\bar{t}H$ events include a high p_T (>150 GeV) or low p_T (<150
503 GeV) Higgs Boson. While this is now a classification model, it uses the same input features
504 described in section 5.4. Binary crossentropy is used as the loss function.

505 **A.5 Impact of Alternative Jet Selection**

506 A relatively low p_T threshold of 15 GeV is used to determine jet candidates, as the jets originating
507 from the Higgs decay are found to fall between 15 and 25 GeV a large fraction of the time. The
508 impact of different jet p_T cuts on our ability to reconstruct the Higgs p_T is explored here. The
509 performance of the Higgs p_T prediction models is evaluated for jet p_T cuts of 10, 15, 20, and 25
510 GeV.

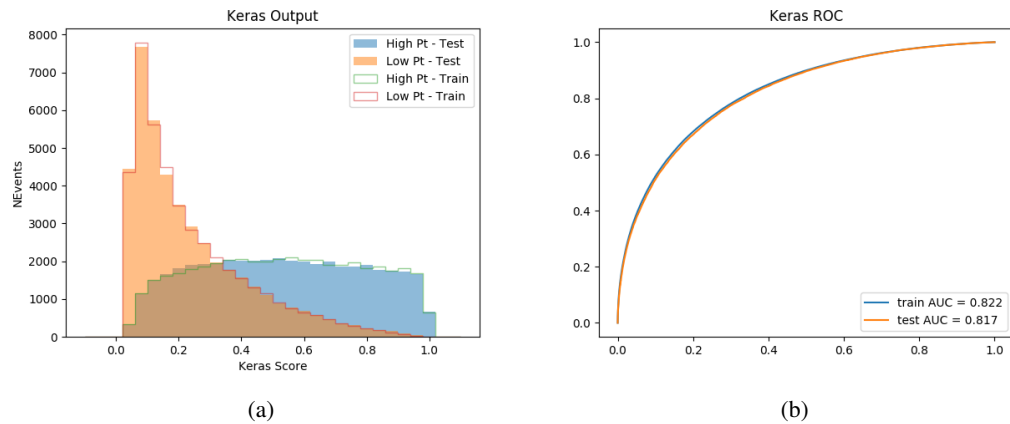


Figure A.26:

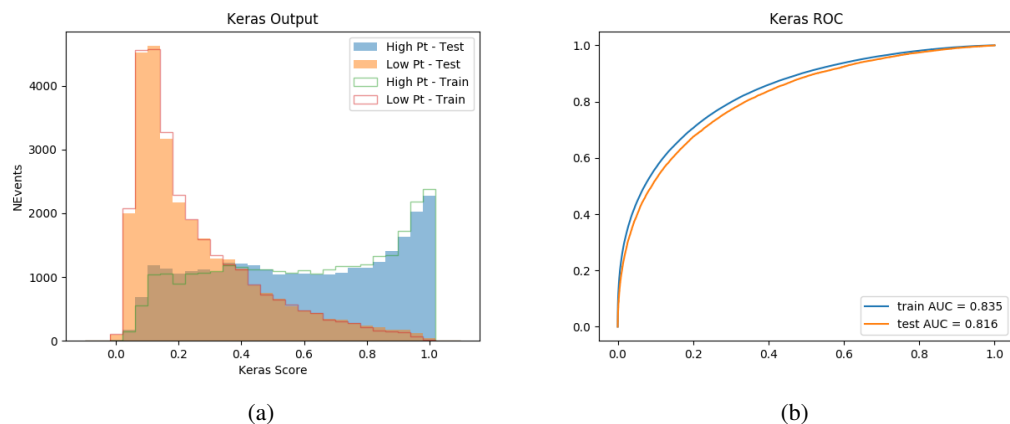


Figure A.27:

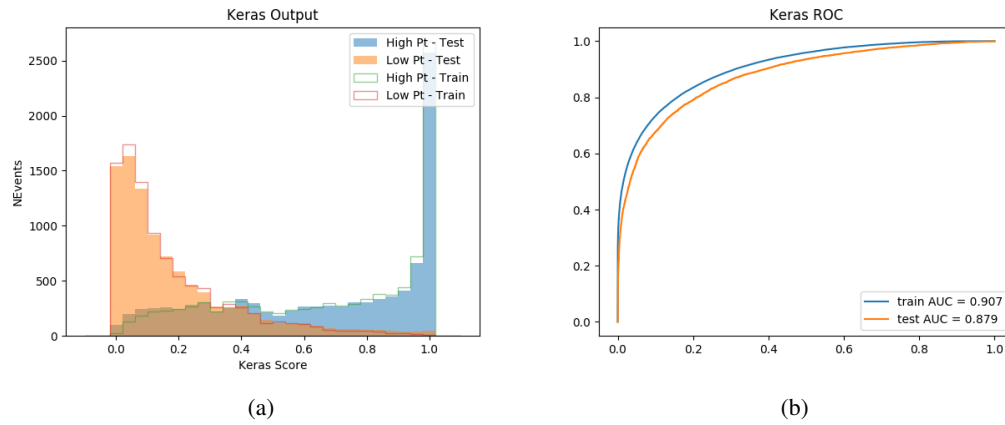


Figure A.28:

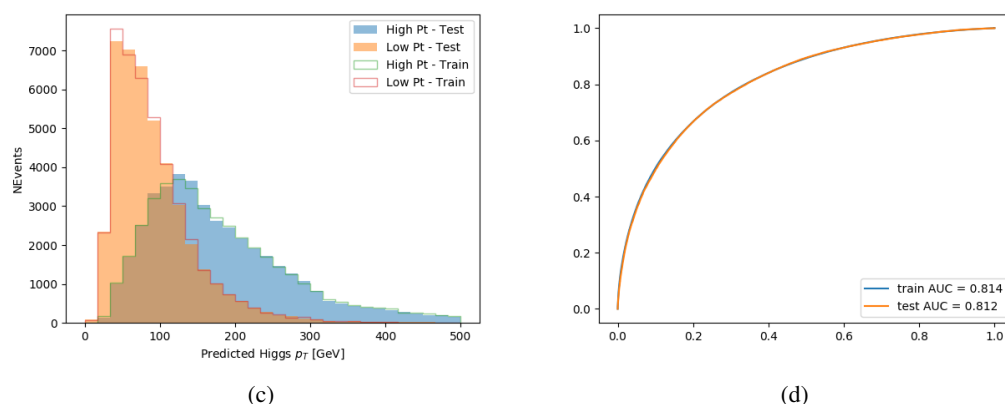
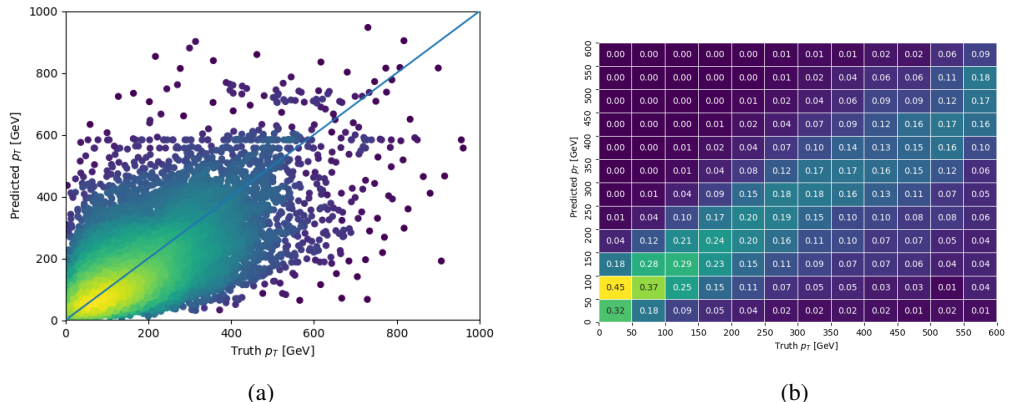


Figure A.29: